This is to certify that the

thesis entitled

The Processing And Characterization
of
FeCrAlY/Al_2O_3 Composites

presented by

Julian E. Ambriz

has been accepted towards fulfillment
of the requirements for

Master of Science degree in Materials Science

Major professor

Date January 30, 1996

THE PROCESSING AND CHARACTERIZATION OF $FeCrAlY/Al_2O_3$ COMPOSITES

By

Julian E. Ambriz

A THESIS

Submitted to

Michigan State University

in partial fulfillment of the requirement

for the degree of

MASTER OF SCIENCE

Department of Materials Science and Mechanics

1996

ABSTRACT

THE PROCESSING AND CHARACTERIZATION
OF
$FeCrAlY/Al_2O_3$ COMPOSITES

By

Julian E. Ambriz

FeCrAlY matrix composites reinforced with FP Al_2O_3 fibers were fabricated using a colloidal suspension process. The process takes advantage of the interparticle forces present when particles are in a liquid medium. By optimizing the suspension pH in accordance with theoretical predictions, the matrix particles are coated onto the fiber eliminating the need for a binder. The processing design allows thoroughly mixed composites with an improved distribution of fiber and matrix to be produced. Matrix powders of different morphology and particle size were used in the composite fabrication and their effects on the fiber volume fraction and distribution were observed. Consolidation was carried out using vacuum hot pressing under various times and pressures to improve fiber alignment and minimize fiber damage as well as achieve full density. Tensile testing was performed at room and elevated temperatures to detect increases in composite strength. Optical microscopy results showed improvements in processing parameters led to increased volume fraction of fiber, improved fiber distribution, and less fiber damage. Tensile data showed some strength improvement. However, low strength values were also evident, mainly due to areas of incomplete consolidation.

DEDICATION

To my family for their love and support

ACKNOWLEDGEMENTS

I would first like to thank the NASA Graduate Researchers Program for providing the funding to support this project. I would also like to thank my advisor, Dr. Melissa Crimp, for her patience and guidance throughout the course of this project,and Dr. Martin Crimp for his technical help and helpful discussion. Special thanks to NASA Lewis Research Center, Cleveland, OH, in particular, Dr. Beverly Aikin, Dr. Mike Nathal, Sue Draper, and Bill Karpinski for their help throughout the project. Finally, I would like to thank Brett Wilson and Dean Oppermann for their help in some of the sample preparation, and the rest of my friends for their encouragement.

TABLE OF CONTENTS

LIST OF TABLES

LIST OF FIGURES

1. INTRODUCTION

The current and future demands of the aerospace and automotive industries require materials to be lightweight, stiff, and able to retain strength at high temperatures. A significant weight to volume reduction coupled with high strength at elevated temperatures allows engines to operate more efficiently. Metal matrix composites (MMCs) are increasingly being used to meet these structural requirements because of the density reduction due to the strength to weight ratio of the reinforcement. However, many areas remain to be investigated before the full potential of these materials can be utilized.

A great potential exists in intermetallics and superalloys for use as matrix materials in advanced composites. They offer high melting points, high elastic moduli, and oxidation resistance at elevated temperatures as well as low densities which are mainly in intermetallics. The disadvantages of these materials lie in low strengths at elevated temperatures and low room temperature ductility, especially in intermetallics. Thus, the need for reinforcement of these materials is apparent.

For structural applications involving unidirectional loading, continuous fiber reinforced MMCs offer a combination of properties which allows the matrix material to display its high melting temperature and oxidation resistance while achieving increased strength from the reinforcement. Fibers are manufactured in large diameters (> 100 μm) and small diameters (<25 μm). Large diameter fibers are in the form of monofilaments or individual fibers while small diameter fibers are multifilament bundles containing up to several hundred filaments per bundle. It is not clear whether large or small diameter fibers are better for optimizing the mechanical properties of composites. In some cases, large diameter fibers allow increases in toughness such as refractory fibers in metals [1] and

many processing methods have been established for incorporating large diameter fibers into metallic matrices. Small diameter fibers are generally stronger due to the lower probability of flaws and have higher aspect ratios (l/d) which allow a large load transfer from the matrix to the fiber. They also provide more flexibility allowing more complex shapes to be produced [2].

Perhaps the most critical aspect to the development of these MMCs is the processing stage. The microstructure, distribution of the reinforcement, fiber/matrix bonding, and the porosity level dictate the mechanical properties of the composite and all of these factors are affected by the processing method. Ideally, the composite would be fully dense and the reinforcement would be uniformly distributed. However, areas containing fiber rich or matrix rich regions are of concern, especially in small diameter fiber reinforced composites [3]. Economic considerations must also be taken into account because the cost of the fibers and matrix powder can be high and many processing routes are complex and slow which lead to increased production costs [4]. Therefore, it is important that the processing methods be cost effective as well as provide optimum mechanical properties.

The objective of this study is to develop the processing techniques necessary to produce fully dense, fine diameter, fiber reinforced MMCs using a binderless, suspension process. The suspension process allows the matrix powder to thoroughly infiltrate the fiber tow resulting in a uniform fiber distribution, eliminating the need for a binder. The composites will be consolidated and characterized to determine the volume fraction of reinforcement, density, fiber distribution and tensile properties. From these results, it will be determined whether this unique processing method provides an efficient and effective means to produce composites with improved strength.

2. LITERATURE REVIEW

2.1 Mechanical Behavior

To better understand the relationship between processing techniques and mechanical properties, it is important to understand the strengthening mechanisms and the basic mechanical behavior of fiber reinforced composites. Although theoretical concepts are not the focus of this project, a basic knowledge of these concepts will allow an understanding of how processing methods can be tailored so mechanical properties can be optimized.

Load Transfer

The primary strengthening mechanism in a fiber reinforced composite is the load transfer between the fiber and matrix. To understand this relationship, Lilholt [5] used the following model to relate the load transfer to the balance of forces during the exchange of load between the fibers and matrix, and the load distribution between them. For the conditions of load transfer, it is assumed there is no change in the external load, the sum of the work is equal to zero and the fiber and matrix are well bonded. Equation 2.1 represents an incremental step of load transfer.

$$(-\sigma_{mt}A_m)\Delta l_{mt} + (\sigma_{ft}A_f)\Delta l_{ft} = 0 \qquad (2.1)$$

During matrix deformation Δl_{mt}, the stress on the matrix decreases by $-\sigma_{mt}$, and during fiber deformation Δl_{ft} the stress on the fiber increases by σ_{ft}. All strains are elastic and the deformations are very small ($\Delta l << l_o$). A_m and A_f represent the cross sectional areas of matrix and fiber respectively. Relating the stress σ and deformation Δl in terms of strain,

Equation 2.1 can be expressed as:

$$(-E_m\varepsilon_{mt})A_m l_0 \varepsilon_{mt} + (E_f \varepsilon_{ft})A_f l_0 \varepsilon_{ft} = 0 \qquad (2.2)$$

or

$$(-A_m l_0)\frac{1}{2}E_m\varepsilon_{mt}^2 + (A_f l_0)\frac{1}{2}E_f\varepsilon_{ft}^2 = 0 \qquad (2.3)$$

where E_x is the elastic modulus and ε_x the strain. Using the relationship between volume, area and original length, and a work parameter describing the relationship between energy and volume,

$$Al_o = volume = v$$

$$W = \frac{1}{2}E\varepsilon^2 = energy/volume$$

Equation 2.3 can be rewritten as:

$$-v_m W_m + v_f W_f = 0 \qquad (2.4)$$

Equation 2.4 shows that transferring the load from the matrix to the fiber requires a large displacement in the matrix and suggests a small displacement in the fiber. If the fibers are required to carry the majority of the load, the stress- strain relationship (modulus) must be higher for the fibers. Thus, the matrix displacement must be larger to balance the force.

Similarly, Lilholt [5] analyzed the load distribution between the fiber and matrix under

elastic deformation. Written in terms of stresses and areas, the total load of the composite is expressed as:

$$A_c\sigma_c = A_f\sigma_f + A_m\sigma_m \tag{2.5}$$

If it is assumed $\varepsilon_c=\varepsilon_m=\varepsilon_f$, rearranging:

$$E_c = \frac{A_f}{A_c}E_f + \frac{A_m}{A_c}E_m \tag{2.6}$$

which can be written as the rule of mixtures for stiffness of a unidirectional composite.

$$E_c = V_f E_f + V_m E_m \tag{2.7}$$

A more detailed analysis of load transfer attributed to Cox [6] by Kelly [7] and Piggot [8] shows the variation of stress along the fiber for an elastic stress transfer. Figure 1 (a) schematically shows a single fiber embedded in a matrix in an unstressed state. As stress is applied, it is assumed that the matrix is strained homogeneously. However, locally along the fiber, the uniform stress and strain is disturbed by the transfer of load as shown in Figure 1 (b). The tensile stress distribution obtained by differentiating the load transfer from the matrix to the fiber is:

$$\sigma = E_f\varepsilon\left(1 - \frac{\cosh\beta((l/2)-x)}{\cosh\beta(l/2)}\right) \tag{2.8}$$

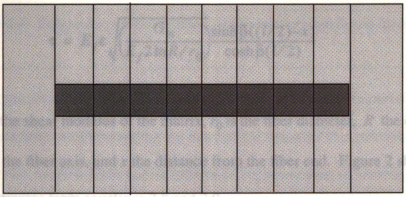

(a)

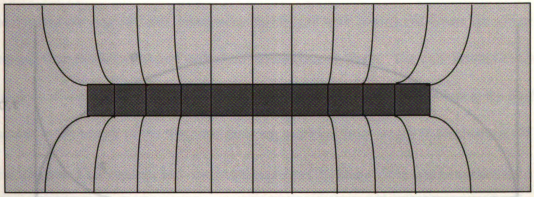

(b)

Figure 1. Single fiber embedded in a composite in an unstressed state (a) and a stressed stated (b). Adapted from [7].

where β is a constant related to the fiber packing array, matrix, and moduli. Similarly, the shear stress τ in the matrix at the fiber-matrix interface is:.

$$\tau = E_f \varepsilon \sqrt{\left(\frac{G_m}{E_f 2 \ln R/r_0}\right)} \frac{\sinh \beta((l/2)-x)}{\cosh \beta(l/2)} \qquad (2.9)$$

where G_m is the shear modulus of the matrix, r_0 is the fiber diameter, R the distance from the center of the fiber axis, and x the distance from the fiber end. Figure 2 shows the variation of the stresses from equations 2.8 and 2.9.

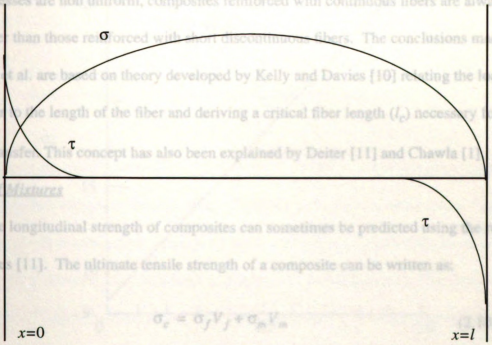

Figure 2. Variation of the tensile stress s and shear stress t along a fiber. Adapted from [8].

The largest tensile stress occurs in the middle of the fiber and the largest values of the shear stress occur at the ends of the fiber, where the shear stress is minimum. From Equations 2.8 and 2.9, Piggot also derived a stress-strain relationship for an idealized composite [8].

Cox's model [6] which shows that the stresses built up along a *discontinuous* fiber in a matrix, is applicable in understanding the mechanical behavior of *continuous* fiber reinforced composite because fibers can be broken during processing or loading. For a *continuous* fiber, Rauch et al. [9] determined the shear stress to be constant along the fiber length and of a low magnitude for uniaxial tension. Similarly, the tensile stress would be constant and equal to the maximum value obtained in a discontinuous fiber. Further analysis by Rauch et al. [9] also determined that because the interfacial shear stresses and fiber tensile stresses are non uniform, composites reinforced with continuous fibers are always stronger than those reinforced with short discontinuous fibers. The conclusions made by Rauch et al. are based on theory developed by Kelly and Davies [10] relating the load transfer to the length of the fiber and deriving a critical fiber length (l_c) necessary for full load transfer. This concept has also been explained by Deiter [11] and Chawla [1].

Rule of Mixtures

The longitudinal strength of composites can sometimes be predicted using the rule of mixtures [11]. The ultimate tensile strength of a composite can be written as:

$$\sigma_c = \sigma_f V_f + \sigma_m V_m \qquad (2.10)$$

where V_f and V_m are the volume fractions of the fiber and matrix, σ_f is the ultimate

strength of the fiber, and σ_m is the ultimate strength of the matrix. The ultimate strength of the composite varies linearly with V_f as shown in Figure 3. However, Equation 2.10 is valid only if the failure strain of the matrix and fiber are equal. In most MMCs where the reinforcement is usually a strong and brittle fiber, the fiber failure strain is much less than that of the matrix. Equation 2.10 is thus modified to:

$$\sigma_c = \sigma_f V_f + \sigma^*_m V_m \tag{2.11}$$

where σ^*_m is the matrix stress when the applied strain reaches the failure strain of the fiber (e' in Figure 4) [12].

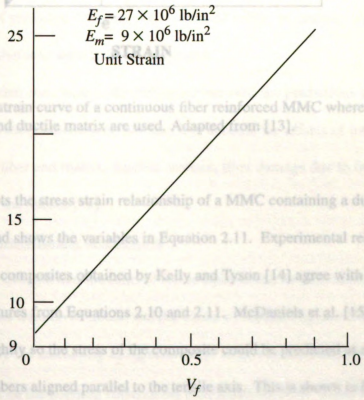

Figure 3. Variation of ultimate strength of MMC with fiber volume fraction V_f. Adapted from [12].

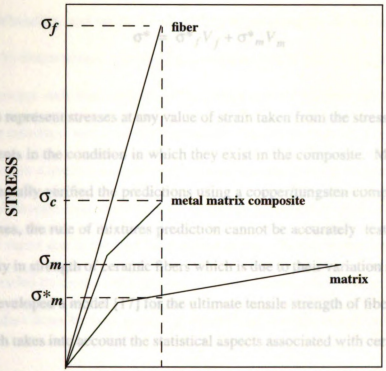

Figure 4. Stress-strain curve of a continuous fiber reinforced MMC where brittle fiber and ductile matrix are used. Adapted from [13].

Figure 4 depicts the stress strain relationship of a MMC containing a ductile matrix and brittle fiber and shows the variables in Equation 2.11. Experimental results from copper/tungsten fiber composites obtained by Kelly and Tyson [14] agree with the prediction of the rule of mixtures from Equations 2.10 and 2.11. McDaniels et al. [15] modified Equation 2.11 slightly so the stress of the composite could be predicted at any strain for composites with fibers aligned parallel to the tensile axis. This is shown in Equation 2.12.

$$\sigma^* = \sigma^*_f V_f + \sigma^*_m V_m \qquad (2.12)$$

The σ*'s represent stresses at any value of strain taken from the stress-strain curves of the components in the condition in which they exist in the composite. McDaniels et al. also experimentally verified the predictions using a copper/tungsten composite. However, in many cases, the rule of mixtures prediction cannot be accurately tested because of the variability in strength of ceramic fibers which is due to their variation in flaw density [16]. Curtin developed a model [17] for the ultimate tensile strength of fiber reinforced composites which takes into account the statistical aspects associated with ceramic fiber strengths. The comparison of predicted strengths with measured values of systems with weak, sliding fiber/matrix interfaces were in good agreement.

Other factors also contribute to the difference between the predictions and experimental results because the predictions do not take into account the effects of interfacial reactions between the fiber and matrix, residual stresses, fiber damage due to fabrication, and the dimensions of the phases [16].

Toughening and Strengthening Mechanisms

Generally, the strength and modulus of the composite can be increased by incorporating a higher volume fraction of fibers, and the extent of toughening due to load transfer can be increased by the increasing E_f/E_m ratio [18]. However, the strength and toughness are also dependent on the bonding between the matrix and the fiber. Thus, the fiber/matrix interface properties have a major effect on the mechanical properties because the load is transferred through the interface.

The properties of interfaces have been characterized by the fracture energy for fiber/matrix debonding, and the frictional sliding stress along the debonded regions [19,20]. Evans [19] characterized a *strongly* bonded interface as one having a large fracture debonding energy such that cracking of the matrix or the fiber does not lead to debonding along the interface, and a *weakly* bonded interface as one having a fracture debonding energy which complies with debonding requirements in the presence of fiber-matrix cracks. Although *weak* interfaces are generally described as ones that debond, their behavior varies due to the frictional sliding stress. These mechanisms have been analytically modeled by Evans and Marshall [20], and Thouless and Evans [21]. The results of these studies describe the mechanical behavior of ceramic matrix or brittle matrix composites.

The requirements for strong and tough composites have been discussed by DiCarlo [22] and Friend [23]. For a brittle matrix composite, a weak interface is desired so that crack propagation will be prevented due to fiber debonding and crack bridging [22] as shown in Figure 5. As the fiber debonds, the amplitude of the stress in the fiber along the matrix crack front is reduced. This allows the crack to bypass the fiber, leaving the fiber intact in the crack wake. The intact fiber inhibits crack propagation and toughening occurs [24]. The sliding resistance τ controls the rate of load transfer from the matrix to the fiber. The mechanisms of fiber bridging and toughening have been well documented [24-27]. For a MMC, a strong interface is required for appropriate load transfer [23] and to allow the ductile matrix to absorb sufficient plastic deformation energy from a propagating crack along the fiber direction [28].

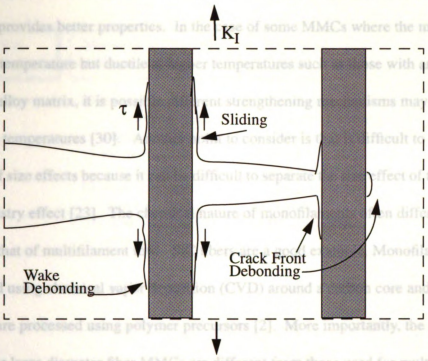

Figure 5. Schematic illustrating the debonding of fibers at the crack front and crack wake. Adapted from [23].

The size of the reinforcement also influences the toughness response [23]. In an investigation of a B/Al system attributed to Signorelli and McDaniels [29] by Friend [23], the toughness increased as the fiber diameter increased. This was due to the extended matrix region around the fiber providing an additional constraint on the fracture when the matrix plastically deformed. DiCarlo [22] stated that large diameter fibers also maximize fiber spacing which can exploit the crack blunting abilities of a ductile metal matrix.

Smaller diameter fibers coupled with a high volume fraction of reinforcement insure enough fibers bridge any matrix cracks in a brittle matrix composite and also decrease the critical fiber length necessary for full load transfer [21]. Additional strength advantages also come from a lower probable flaw density [2].

As previously mentioned, it is not clear whether or not which type of fiber reinforcement provides better properties. In the case of some MMCs where the matrix is brittle at room temperature but ductile at higher temperatures such as those with an intermetallic or superalloy matrix, it is possible different strengthening mechanisms may be active at different temperatures [30]. Another point to consider is that is difficult to make a true analysis of size effects because it can be difficult to separate the size effect of the fiber from the chemistry effect [23]. The chemical nature of monofilaments often differ significantly from that of multifilament tow. SiC fibers are a good example. Monofilaments are processed using chemical vapor deposition (CVD) around a carbon core and multifilament tows are processed using polymer precursors [2]. More importantly, the processing methods for large diameter fiber MMCs are different from those used for multifilament MMCs and thus the microstructures produced will differ because the fiber distributions will be varied as well the porosity level, or any segregation effects in the matrix [23].

Tensile Behavior

To better understand the mechanical properties in relation to the structure and processing required, Ochiai [31], and Ochiai and Osamura [31-36], examined the factors affecting the tensile behavior of unidirectional fiber reinforced MMCs. Through the use of a computer aided Monte Carlo simulation method, the behavior of the composite was predicted. The simulation method was used as a means to overcome some experimental difficulties due to the many factors involved in the tensile strength of unidirectional MMCs. When one component is varied, the other factors also vary [31]. Figure 6 shows the factors affecting the tensile strength.

The tensile strength of fiber reinforced MMCs has been predicted in relation to

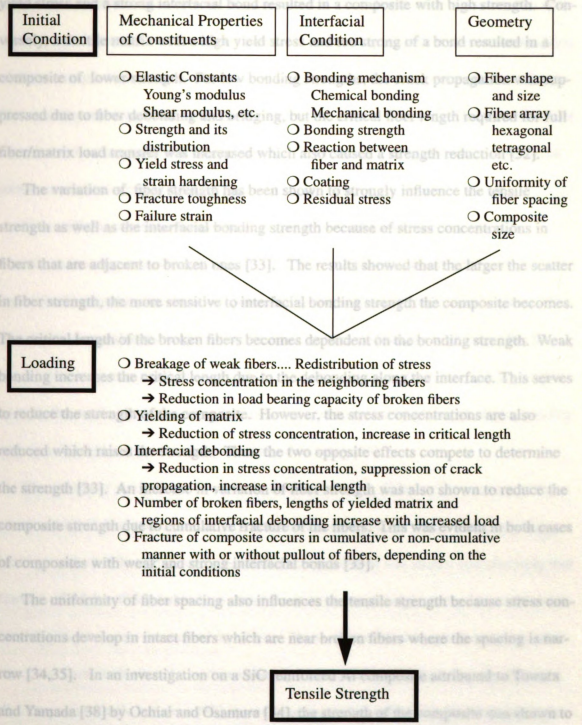

Figure 6. Factors affecting the tensile strength of a unidirectional MMC. Adapted from [31].

interfacial bonding strength and the matrix ductility [32]. A ductile matrix with a low yield stress and a strong interfacial bond resulted in a composite with high strength. Conversely, a ductile matrix with a high yield stress and too strong of a bond resulted in a composite of lower strength. For low bonding strengths, the crack propagation was suppressed due to fiber debonding and bridging, but the critical fiber length required for full fiber/matrix load transfer was increased which also caused a strength reduction [32].

The variation of fiber strength has been shown to strongly influence the tensile strength as well as the interfacial bonding strength because of stress concentrations in fibers that are adjacent to broken ones [33]. The results showed that the larger the scatter in fiber strength, the more sensitive to interfacial bonding strength the composite becomes. The critical length of the broken fibers becomes dependent on the bonding strength. Weak bonding increases the critical length due to the debonding along the interface. This serves to reduce the strength of the composite. However, the stress concentrations are also reduced which raises the strength. Thus, the two opposite effects compete to determine the strength [33]. An increase in variation of fiber strength was also shown to reduce the composite strength due to cumulative fracture of the fibers. This was evident in both cases of composites with weak and strong interfacial bonds [33].

The uniformity of fiber spacing also influences the tensile strength because stress concentrations develop in intact fibers which are near broken fibers where the spacing is narrow [34,35]. In an investigation on a SiC reinforced Al composite attributed to Towata and Yamada [38] by Ochiai and Osamura [34], the strength of the composite was shown to improve by increasing the fiber separation. This an important factor to consider since multifilament fibers are supplied in a bundle and composites reinforced with them usually

tend to contain a relatively non-uniform spacing. Results from the Monte Carlo simulation study by Ochiai and Osamura [35] showed that the strength of composites with non uniform spacing was lower than those with uniform spacing. Furthermore, as the variation of fiber strength increased, the difference in strength between composites with uniform fiber spacing and those with non uniform fiber spacing also increased. This was due to the cumulative fracture mode for a large scatter in fiber strength coupled with the increased stress concentrations in areas with narrow fiber spacing.

Non-uniform interfiber spacing can also contribute to interfacial damage. In MacKay's investigation of a SiC fiber/Ti-15V-3Cr-3Al-3Sn composite [39], radial cracking at the fiber/matrix interface was prevalent between fibers spaced closer together. The investigation revealed the majority of the cracking occurred during cooldown after hot consolidation. It was not determined at the time what kind of effect the cracking would have on the mechanical properties, but the cracks could probably propagate during loading and thus should be considered as potentially damaging [39].

The effects of stress concentrations in fibers containing different diameters were also examined by Ochiai and Osamura [36] because the diameters of fibers is also characterized by a size distribution in many functional composites. It was shown quantitatively that fracture of thicker fibers led to high stress concentrations in neighboring thinner fibers resulting in premature fracture of the thinner fibers. The critical length for load transfer was also larger in thicker fibers, thus reducing load transferring efficiency. Modeling of the composite tensile behavior [37] showed the larger the variation in fiber diameter, the lower the composite strength. The model used could not be directly applied to practical composites because the size of the model was much smaller in comparison to actual

composites and the fiber configuration used for the model is not regularly found [37].

Elevated Temperature Considerations

It is important that the tensile strength be maintained at elevated temperatures if the composite is to undergo any elevated temperature usage. However, at these temperatures the strength of the composite is usually reduced because the interfacial strength is affected by reaction products or fiber strength degradation occurring during isothermal exposure [40,41], or by reduction in the load carried directly by the matrix since the strength of metals typically decreases at elevated temperatures.

Wright and Intwala [40] investigated the effects of elevated temperatures on B/Al composites. Exposing the composites to 600° C over increasing periods of time reduced the tensile strength significantly. An initial pronounced drop in strength was followed by a gradual decrease in strength with time up to four hours. Prolonged exposure at 600°C resulted in a reaction layer at the fiber/matrix interface and a corresponding decrease in modulus was observed.

Kyono et al. [41] examined the toughness of B/Al composites after exposure to 500°C and found that the toughness decreased with increased exposure time. TEM, SEM, and X-Ray analysis revealed AlB_2 reaction products on the fiber. Tensile tests on the fibers revealed a decrease in strength directionally proportional to exposure time as a result of the formation of reaction products.

The preceding discussions showed that many factors affect the tensile behavior of fiber reinforced MMCs, and they can be adjusted or improved through careful material selection and the processing method (which is the focus of this study). In the following sections, fabrication processes for continuous fiber reinforced MMCs will be discussed along

with the importance of consolidation parameters and fiber damage during processing, the theory behind the process used for this study, and the selection of the materials used in the research project.

2.2 Processing Methods

A wide range of methods are used to fabricate fiber reinforced MMCs. Thermal spray [42-46], foil-fiber-fiber [44,45], powder cloth [44,45], and vapor deposition [42, 44, 47] methods are used to make preformed sheets or plies which are then consolidated by hot pressing. Liquid methods such as pressure casting involve infiltrating fibers or fiber preforms with molten metal [44,47-49].

Thermal Spray Methods

A thermal spray operation such as arc spraying or plasma spraying involves spraying molten metal onto a single layer of fibers wound on a drum to form a monotape. The monotapes are then cut, stacked and consolidated into panels or shapes by vacuum hot pressing (VHP) or hot isostatic pressing (HIP). The process is usually performed in an atmosphere controlled chamber to prevent oxygen contamination [42-45]. An arc spray process is schematically shown in Figure 7. The composite monotapes are formed by melting a wire of the matrix by means of an electric arc between the wire and a cathode located in the spray head. The molten drops are then sprayed onto the fibers wound on the drum in a controlled atmosphere. The drum is rotated and translated to provide a uniform coating [43]. The technique is used to fabricate tungsten fiber reinforced superalloys.

The plasma spray process differs from the arc spray process in the spraying device and the form of matrix material used [44]. Molten particles are produced using prealloyed powder instead of a wire feedstock and plasma forming gases such as Ar, He, N_2, and H_2

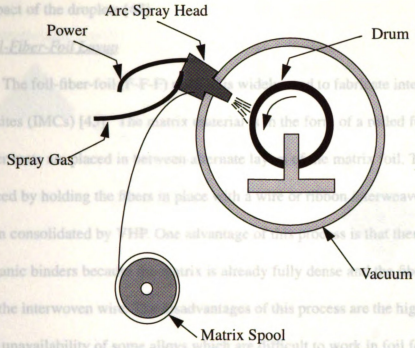

Figure 7. Schematic of arc spray process. Adapted from [41].

are injected between two electrodes which produces the plasma flame to melt the powder. The device is widely used and can be used to spray all materials onto any substrate [44].

The main advantages of these two methods are that fibers can be uniformly spaced and no organic binders are used which eliminates any potential contamination and added processing time for binder removal [45]. In addition, plasma sprayed films show higher hardness than do pure metal films because of the rapid cooling of the metal droplets when they make contact with the fiber [44].

The disadvantages of thermal spray processes are that they are limited to large diameter fibers and can be expensive [45]. The arc spray process is limited because of the limited availability of the matrix material in the form of a wire. Plasma spray coatings also

tend to have porosity and greater surface roughness [46] and fibers may be damaged by the impact of the droplets [47].

Foil-Fiber-Foil Layup

The foil-fiber-foil (F-F-F) method is widely used to fabricate intermetallic matrix composites (IMCs) [45]. The matrix material is in the form of a rolled foil and unidirectional fiber mats are placed in between alternate layers of the matrix foil. The fiber mat is produced by holding the fibers in place with a wire or ribbon interweave. The composite is then consolidated by VHP. One advantage of this process is that there is no need for organic binders because the matrix is already fully dense and the fibers are held in place by the interwoven wire. The disadvantages of this process are the high cost of the foils and the unavailability of some alloys which are difficult to work in foil form [47]. The interweave material must also be the same composition of the matrix to avoid any damaging chemical reactions [47].

Powder-Cloth Process

The powder cloth process is used to fabricate IMCs and is schematically shown in Figure 8 [45]. The prealloyed matrix powder is mixed with a binder and wetting agent. Then the mixture is rolled into thin sheets or cloths which are cut to the specimen dimensions. The fiber mat is made by winding the fibers onto a drum and coating them with another binder. The mats are then cut to size and stacked in alternating layers and consolidated by VHP. The advantage of this process is that matrix powders are readily available making it applicable to a wide range of materials. The disadvantages of this process are that accurate fiber spacing is difficult [47] and the potential contamination problems associated with binders such as toxic by-products and residue after consolidation [45].

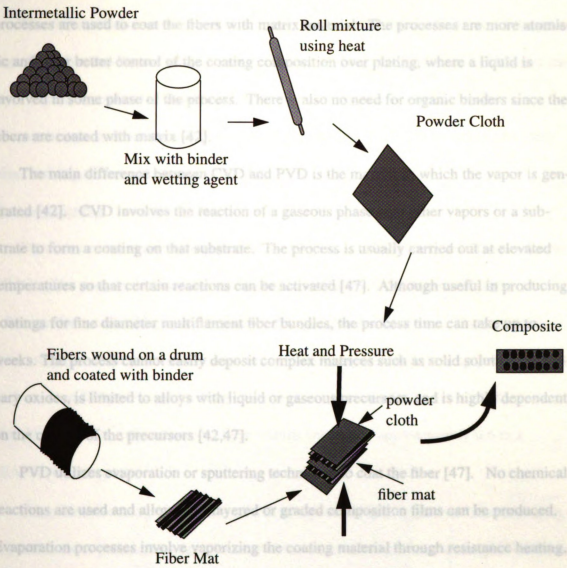

Figure 8. Schematic of powder cloth process. Adapted from [45].

Vapor Deposition Methods

Chemical vapor deposition (CVD) [42,47] and physical vapor deposition (PVD) [42] processes are used to coat the fibers with matrix material. The processes are more atomistic and offer better control of the coating composition over plating, where a liquid is involved in some phase of the process. There is also no need for organic binders since the fibers are coated with matrix [42].

The main difference between CVD and PVD is the manner in which the vapor is generated [42]. CVD involves the reaction of a gaseous phase with other vapors or a substrate to form a coating on that substrate. The process is usually carried out at elevated temperatures so that certain reactions can be activated [47]. Although useful in producing coatings for fine diameter multifilament fiber bundles, the process time can take up to weeks. The process cannot easily deposit complex matrices such as solid solutions or ternary oxides, is limited to alloys with liquid or gaseous precursors, and is highly dependent on the control of the precursors [42,47].

PVD utilizes evaporation or sputtering techniques to coat the fiber [47]. No chemical reactions are used and alloy, multilayered or graded composition films can be produced. Evaporation processes involve vaporizing the coating material through resistance heating, electron beam evaporation, or radiation heating, and then depositing it onto a substrate [42]. Sputtering utilizes techniques where the coating material is a target or cathode and vaporized through a momentum transfer in a gas glow discharge. Vapor sources include magnetrons or ion beam guns [42]. PVD contains several advantages. Lower temperatures are required than CVD which can be useful in fabricating composites with reactive matrices such as Al/C where carbides might form [47]. There is also the potential for

more versatility in the microstructure and composition of the coating because coatings can come from pure metals, compounds, or alloys from alloy targets.

The volume fraction of the matrix is controlled by adjusting the thickness of the coating. Partridge and Ward-Close [47] obtained fiber volume fractions of up to 80% and uniform fiber spacing for Ti-6Al-4V/SiC composites. Despite the control over the microstructure and versatility, the machinery required for PVD can be costly and complex, and deposition rates can be slow [42].

Pressure Casting

Pressure casting is commonly used in the fabrication of fine diameter fiber reinforced MMCs. The process is schematically illustrated in Figure 9. Molten metal is poured over a fiber preform and infiltration is forced by the application of pressure. The composite is then solidified under pressure. The process is widely used for low melting point matrices such as Al and Mg [47] and has been successful in producing IMCs as well [48]. Nourkbakhsh et al. [48] achieved a fiber volume fraction of approximately 0.6 in a $NiAl/Al_2O_3$ composite.

The pressure casting process has the advantage of being inexpensive. However alloying additions or precoating of the fibers are often required to promote wetting of the fiber by the molten metal [47]. Liu and Chao [49] have found the addition of Mg to an Al matrix improves infiltration and decreases porosity of the composites. It was also found that increased additions of Mg increased the tensile strength of the composites. Composites produced by this method tend to contain a large variation in fiber spacing and frequent fiber/fiber contact or fiber bonding [47,49].

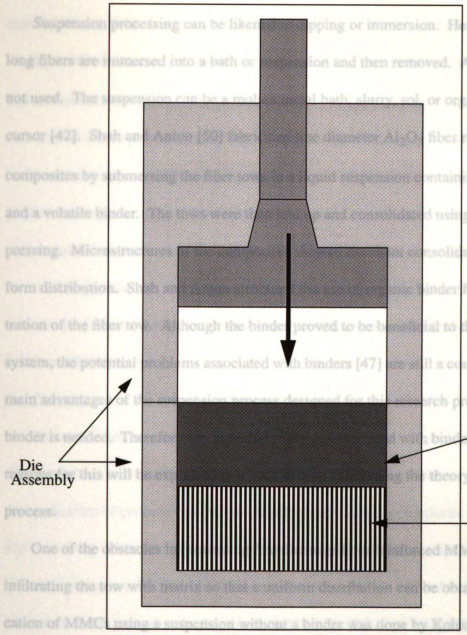

Figure 9. Schematic of pressure casting process.

Suspension Process

Suspension processing can be likened to dipping or immersion. Here, continuous or long fibers are immersed into a bath or suspension and then removed. A fiber preform is not used. The suspension can be a molten metal bath, slurry, sol, or organometallic precursor [42]. Shah and Anton [50] fabricated fine diameter Al_2O_3 fiber reinforced NiAl composites by submersing the fiber tows in a liquid suspension containing matrix powder and a volatile binder. The tows were then laid up and consolidated using low pressure hot pressing. Microstructures of the composites showed excellent consolidation and a uniform distribution. Shah and Anton attributed the use of organic binder for efficient infiltration of the fiber tow. Although the binder proved to be beneficial to this particular system, the potential problems associated with binders [47] are still a concern. One of the main advantages of the suspension process designed for this research project is that no binder is needed. Therefore any potential problem associated with binders is avoided. The reasons for this will be explained in a later section concerning the theory involved in the process.

One of the obstacles in processing fine diameter fiber reinforced MMCs is thoroughly infiltrating the tow with matrix so that a uniform distribution can be obtained. The fabrication of MMCs using a suspension without a binder was done by Kohara and Moto [51] for SiC fiber reinforced aluminum. The suspension contained aluminum powder and sodium alganate which was used as a dispersant. There was considerable difficulty in infiltrating the fiber tows. Crevices remained inside the bundle leading to problems with residual pores.

A unique processing technique was developed by Wilson et al. [52], and Suydam [53]

to produce continuous fiber reinforced IMCs using a binderless, suspension process developed by Crimp [54], Crimp et al. [55], Wilson [56], and Wilson and Crimp [57]. FP Al_2O_3 multistrand tows were drawn through a FeAl suspension containing matrix powder and an electrolyte solution. The results showed a uniform coating of matrix on the fibers and the tow thoroughly infiltrated with matrix powder. This was accomplished by theoretically examining the matrix and fiber interactions with the aid of a computer program to predict the suspension conditions at which the matrix would adhere to the fiber. Although only a green compact was produced, the results provided enough evidence that a composite could be produced in this manner. The process design is the same one used for this research project and the theory behind it will be discussed in Section 2.4.

2.3 Consolidation

Hot Pressing

The most common method used to consolidate MMCs is hot pressing which is usually carried out in an inert atmosphere or vacuum. The process achieves bonding through the application of pressure and temperature and enhances the composite density by removing voids [44]. The main parameters of interest are temperature, pressure and time. Some typical pressing conditions used are temperatures from 50 to 90% of the matrix solidus temperature and pressures ranging from 15-110 MPa (2.2-15.9 ksi) [42].

The consolidation conditions have a great effect on the composite properties and it is important to understand the processing history in order to understand the material properties [39]. In optimizing the composite's performance, the best parameters must be selected. Bhagat [58] examined the effects of hot pressing parameters on the strength of Al/stainless steel composites. The change in tensile strength was correlated with

variations in temperature, pressure, and time. One parameter was varied while the other two were held constant. Composites fabricated under optimum processing conditions showed an ideal interface with good metallurgical bonding and an improved tensile strength over that predicted by the rule of mixtures for up to 40% of fiber volume fraction.

Information on processing parameters is available in open literature, but some is limited mainly for the following reasons: government restrictions and commercial distributors that consider the fabrication process as proprietary information [42] in order to retain their competitive edge. The federal government has recognized MMC processing technology as vital to national security interests and prevents distribution of this information to foreign nationals without a valid export license [42].

Fiber Damage

One of the major problems in the manufacture of fiber reinforced MMCs is fiber damage [59]. Several models [59-63] have been developed to describe the factors involved in fiber fracture during consolidation. Nicalou et al. [59] developed a model to describe the cause of fiber fracture in MMCs consolidated from foil-fiber-foil layups. Fiber breakage during consolidation was shown to occur due to bending induced by cross weave wires. The model also verified that breakage may occur at low levels of pressure such as those applied to keep the fiber mats in place during the initial heat-up prior to consolidation. Nicalou et al. proposed several guidelines to avoid fiber fracture during foil-fiber-foil MMC processing: the use of smaller diameter fibers so the Weibull modulus and bending strength will be increased, and smaller diameter cross weave wire or thin cross weave ribbon to minimize the stress concentrations.

Elzey et al. [60] and Groves et al. [61] examined the causes of fiber fracture in plasma

sprayed MMC monotapes. The monotapes were SCS-6 SiC fiber reinforced, Ti based composites. Both studies showed fiber fracture to occur due to stress concentrations created in the fiber when it comes in contact with an asperity. Elzey et al. [52] developed a model to predict the number of fractures that occurred during consolidation and simulate fractures which occur due to fiber bending. The results from the investigation by Groves et al. [53] showed the density of fiber fractures to be directly proportional to the application pressure and inversely proportional to the processing temperature. The study also used a model to predict that increases in fiber strength, diameter and stiffness; decreases in matrix yield and creep strength and decreases in monotape surface roughness will lower the fiber fracture density.

Koss et al. [54] analyzed fiber fracture in sapphire reinforced MMCs. The basis of the analysis was that fiber fracture occurred during consolidation as a result of tensile stresses generated in the fibers due to metal flow along the fiber axis. The matrix flow creates tensile stresses in the fiber large enough to fracture the fiber into fragmented lengths. A model of this probable cause of fiber fracture was developed for two cases: the case in which fiber bonding occurs and the case where fiber matrix bonding does not occur and frictional sliding is present. In both cases the ratio of the fiber strength to matrix yield strength was critical to controlling the fragmentation length. The predictions were compared to experimental observations for a variety of composite systems and were found to be in good agreement. Koss et al. also suggested conditions which should minimize fiber fracture during processing such as using a soft, compliant interlayer, hot pressing such that the fibers are positioned transverse to the die channel so the matrix will not flow in the fiber direction, and hot pressing at a temperature high enough where the flow stress of the

metal is low. However, the fiber strength degradation due to thermomechanical interactions with the matrix and interlayer must be evaluated and the analysis by Koss et al. ignored these other forms of fiber damage.

Warren et al. [63] investigated the fiber damage during the consolidation of PVD coated, fine diameter Al_2O_3 fibers. The fiber tows were coated with a Ti-6Al-4V matrix and then consolidated using HIP and interrupted VHP cycles. The VHP cycles were varied to examine the effect of the loading rate on the fiber damage during the early stages of consolidation. The results from fragmentation analysis showed that fiber damage was significantly lower when the processing load was applied gradually or at a slower rate. The fiber damage mechanisms identified were microbending and fracture of the fiber and reaction between the fiber and matrix. A model was developed to understand the observed fiber damage by simulating the fiber bending and failure mechanism in a representative unit cell. From the model and experimental observations, it was concluded that in order to consolidate the system while avoiding fiber breaks the processing cycle must be designed so that there is sufficient time for matrix creep to eliminate void volume within the specimen. This could be accomplished if the time frame required to transfer the matrix to the void space is within the timeframe of the cycle, the necessary matrix strain rates are attainable at loads which do not cause excessive fiber bending, significant matrix grain growth is inhibited during processing, and fiber strength is retained during high temperature processing.

2.4 Suspension Process Theory

The theory behind the suspension process used for this study is based on colloidal theory concerning interparticle forces, surface energies and their interaction. Forces acting

upon particles include repulsive forces due to electrical charges on the particle's surface, van der Waals attractive forces and stearic forces occurring from adsorbed solvent on the particles [64]. The stearic forces can be caused by the addition of copolymers which are adsorbed by the particles [65]. However, the suspension used in this study does not contain copolymers so the effect of these forces will not be considered. Balancing the attractive and repulsive forces determines the *stability* of the suspension. Stability can be defined by the amount of flocculation or coagulation that takes places within a suspension. A suspension is considered *stable* if the particles within are dispersed. Conversely, an *unstable* suspension is one in which flocculation occurs. The following subsections briefly discuss the main points of the colloid theory involved in this process. A more in-depth review of the theory can be found in literature by Heimenz [64], Hunter [65], and Shaw [66].

Electrokinetic Phenomena

When particles are immersed in a liquid medium, they spontaneously ionize and acquire a surface charge [66]. This is schematically shown in Figure 10. In this case, fibers and matrix powder particles are used to illustrate the application toward a composite system. Ideally, the fibers lie parallel, not crossed. Each particle acquires a distribution of ions or an "ionic cloud" which is known as an electric double layer. The electric double layer consists of an inner region that includes ions adsorbed at the particle's surface and a diffuse outer region in which ions are distributed according to the influence of random thermal motion and electrical forces [66]. The thickness of the double layer extends from the particle surface and is measured by a parameter known as the Debye-length [67].

The combination of particle motion in the fluid medium and the electrical effects on

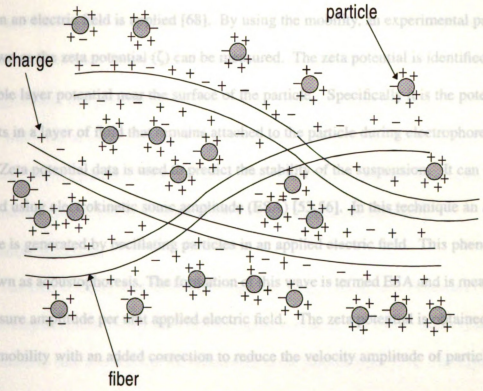

Figure 10. Schematic illustrating particle interactions and surface charges that develop when components are immersed in a suspension.

the particle result in electrokinetic phenomena [68]. Several types of electrokinetic phenomena exist, but only one type, electrophoresis, will be discussed because it is relevant to the process used for this study.

Electrophoresis describes the movement of charged particles in a colloidal suspension when an electric field is applied [68]. By using the mobility, an experimental parameter known as the zeta potential (ζ) can be measured. The zeta potential is identified with the double layer potential near the surface of the particle. Specifically it is the potential that exists in a layer of fluid that remains attached to the particle during electrophoresis [68].

Zeta potential data is used to predict the stability of the suspension. It can be measured using electrokinetic sonic amplitude (ESA) [53,56]. In this technique an acoustic wave is generated by oscillating particles in an applied electric field. This phenomena is known as acoustophoresis. The formation of this wave is termed ESA and is measured as a pressure amplitude per unit applied electric field. The zeta potential is obtained by using the mobility with an added correction to reduce the velocity amplitude of particle motion [57].

DLVO Theory

A theory developed by Deryaguin, Landau, Verwey, and Overbeek (DLVO) [69,70] explains the interaction between particle double layers of length $1/\kappa$ which provide stability against flocculation. The theory is based on the electrostatic repulsive forces and attractive forces present in a colloidal suspension. The total energy that exists between two particles is the sum of the attractive and repulsive forces.

$$V_t = V_r + V_a \tag{2.13}$$

where V_r is the repulsive force due to overlapping of the diffuse double layer and V_a is the attractive force due to Van der Waals forces. This is graphically shown in Figure 11. When particles approach each other and their double layers overlap, a repulsive force is created and the range of repulsive interaction depends on the double layer thickness. The Van der Waals forces have a particular range of attraction as well. If the particles get too close to one another, they adhere and form agglomerates. The total force V_t represents the energy barrier that prevents flocculation. If the repulsive forces dominate, a stable suspension will exist as shown in Figure 11. If the attractive forces dominate, flocculation occurs. The magnitude of these forces can be controlled by altering the suspension parameters such as pH, electrolyte concentration, and temperature [67].

Stability Predictions

The DLVO theory was further developed by Hogg, Healey and Furstenau (HHF) [71] to develop a stability theory for a multicomponent system. The theory uses expanded force equations to take into account the differences in the particle types [57]. The expression for the attractive force is:

$$V_a = \frac{-A}{12}\left[\frac{y}{x^2+xy+x} + \frac{y}{x^2+xy+x+y} + 2\log\frac{x^2+xy+x}{x^2+xy+x+y}\right] \qquad (2.14)$$

where A is the Hamaker constant which is calculated in order to determine the attractive force due to Van der Waals forces. The variables x and y are functions of interparticle distance and particle radii. The expression for the repulsive force for HHF is:

$$V_r = \varepsilon_0\varepsilon_r\pi\left(\frac{a_1a_2}{(a_1+a_2)}\right)\left(\Psi_{0_1}^2+\Psi_{0_2}^2\right)\times\left[\frac{2\Psi_{0_1}\Psi_{0_2}}{\Psi_{0_1}^2+\Psi_{0_2}^2}\ln\frac{1+\exp{-\kappa H}}{1-\exp{-\kappa H}} + \ln(1-\exp(-2\kappa H))\right] \qquad (2.15)$$

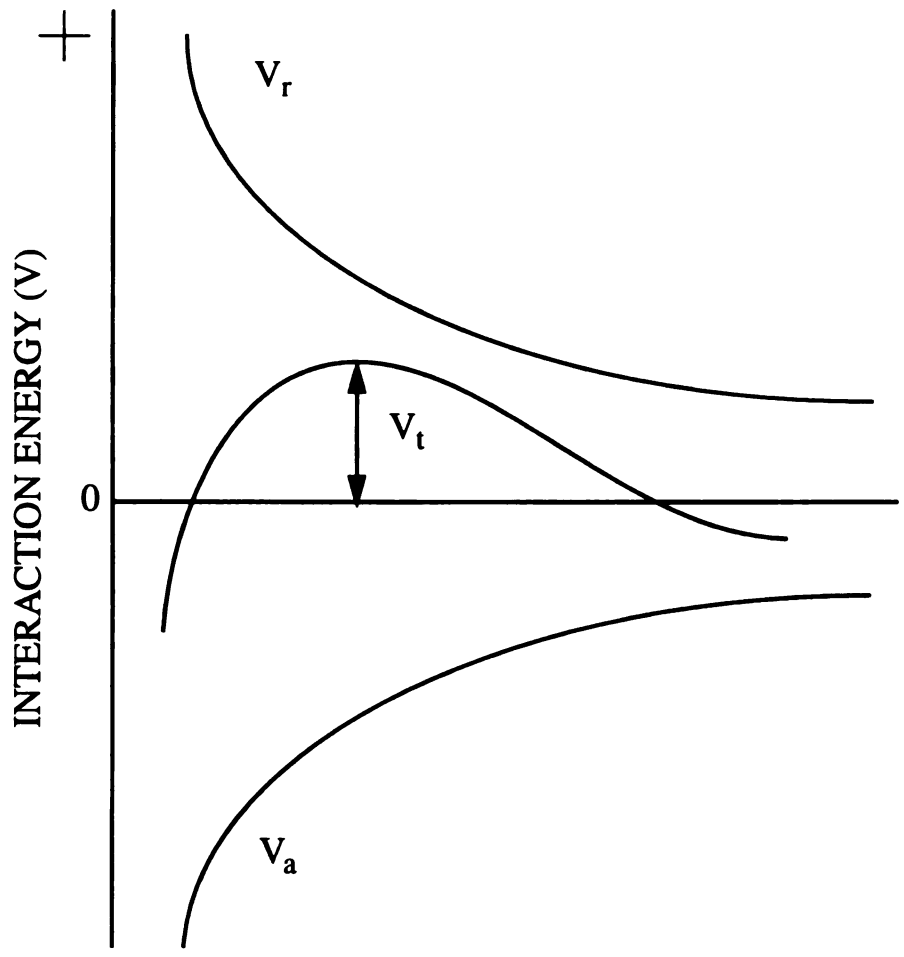

Figure 11. Plot representing the interaction of particle forces indicating a stable suspension.

where Ψ_0 is the particle potential, ε_0 is the permittivity in a vacuum, ε_r is the relative permittivity, H the interparticle distance, and κ the Debye-Huckel parameter. By adding Equations 2.14 and 2.15, the total interaction energy as a function of interparticle distance for two spherical particles that are not identical can be calculated [57].

From HHF theory, a computer program, *Suspension Stability*©, was developed by Wilson [59] to predict the stability of ceramic composite systems. The program was also used in Suydam's work [53] and in this research project. The program takes zeta potential and other system and material data (particle size, Hamaker constant, pH and electrolyte concentration) and calculates the stability prediction. The results are defined by a stability ratio W and describe the interactions between the matrix particles themselves, the fibers themselves and the interaction between the fiber and matrix. The overall stability W_T can be defined as:

$$W_T = \left[\frac{n^2}{W_{11}} + \frac{(1-n)^2}{W_{22}} + \frac{2n(1-n)}{W_{12}}\right] \qquad (2.16)$$

where W_{11} is the stability of the matrix particles themselves, W_{22} the stability of the fibers themselves and W_{12} the stability of the matrix and fibers with respect to each other. The results are plotted as log (W) vs. pH. Stability is defined as log (W) values greater than 10 [57].

The goal here is to predict the conditions at which the matrix powder will be stable and adhere to the fiber, and the fibers will remain spread so the powder particles can infiltrate the tows. By taking advantage of the interparticle forces present, fiber coating can be accomplished without the aid of an organic binder.

2.5 Material Selection

The main benefits of ceramic fibers as reinforcements for advanced composite materials are their high temperature strength and modulus as well as their resistance to environmental degradation. However, in choosing a suitable reinforcement there are two major factors to consider, the chemical compatibility with the matrix and the difference in thermal expansion between the fiber and matrix (coefficient of thermal expansion (CTE) mismatch). A large difference in thermal expansion can result in cracking at the interface due to the build up of thermal stresses [1]. Chemical reactions at the fiber/matrix interface can also occur during processing and significantly reduce the strength of the composite [31].

Several studies on the chemical compatibility of ceramic reinforcements with intermetallics [72-74] have been conducted to determine the feasibility of these materials as composites. Yang et al. [72] prepared diffusion couples of intermetallic compounds with various reinforcement materials by vacuum hot pressing. The chemical compatibility between the materials was then analyzed in the as received state and after prolonged heat exposure. The results summarized in Table 1 provided a qualitative description of the bonding in terms of reactivity and whether or not the reinforcements bonded or debonded. From these results, the most favorable reinforcements appear to be Al_2O_3, Y_2O_3, and TiB_2 which exhibited good bonding with most of the matrices and no chemical reaction occurred. It was also concluded that the CTE mismatch between the intermetallic compounds and the SiC/Si_3N_4 reinforcements may have led to the debonding of those materials.

A similar compatibility study was performed by Shah et al [73], but with more focus on the overall composite microstructure in terms of uniformity, fiber damage, and the

Table1. Interaction between intermetallic compounds and reinforcements. The abbreviations B-bonded, D-debonded are used for the bond character and R-reacted, NR-nonreacted are used for reactivity. Adapted from [72].

Intermetallics	**Reinforcements**					
	SiC	TiC	Si_3N_4	Al_2O_3	Y_2O_3	TiB_2
Cr_3Si	D, NR	B, NR	D, NR	D, NR	B, NR	B, NR
Co_2Nb	D, NR	B, R	D, NR	B, NR	B, NR	D, NR
Cr_2Nb	D, NR	B, R	D,NR	B, NR	B, NR	B, NR
Nb_2Al	D, NR	B, NR	D, NR	B, NR	B, NR	D, NR
$MoSi_2$	D, NR	B, NR	D, NR	B, NR	B, NR	B, R

microporosity. The intermetallic compounds used included NiAl, a complex niobium based alloy NbX-15, and ternary titanium aluminides (Nb, Ti)$_2$Al and (Nb, Ti) Al_2. The reinforcements were Al_2O_3, SiC, Si_3N_4, TiC, and Y_2O_3. The composites were processed by vacuum hot pressing pre-alloyed powder blended with the reinforcements. The observations were summarized in terms of the attractive features and potential problems of the reinforcement. The Al_2O_3 reinforcements, FP multistrand fibers and Saphikon® monofilaments, were found to be most attractive in that they were chemically stable in almost all the systems, showed no interdiffusion and exhibited a weak to strongly bonded interface.

The favorability of Al_2O_3 fibers was further shown by Draper et al. [74] in a compatibility study of intermetallic Fe-40Al (at%) with various large diameter fibers. Composites were fabricated using Al_2O_3, SiC, B, W, and Mo-based fibers as reinforcements and their compatibilities with the matrix were investigated using thermodynamic calculations and experimental verification. A summary of the thermodynamic calculations showed

Al_2O_3 to be completely compatible with Fe-40Al because no reaction products were expected to form. Similarly,W was also found to be compatible even though 2% solubility of W in Fe-40Al was expected at 1500K. The microstructures for both composites showed no visible reaction products after fabrication. However, after heat treatment for 25 h at 1500K, the W/Fe-40Al samples contained porosity attributed to a Kirkendall effect whereas the Al_2O_3/Fe-40Al samples showed no reaction. The density of Al_2O_3 is much lower than W (3.96 g/cc for Al_2O_3, 19.3 g/cc for W) and the CTE (9.4×10^{-6}/K for Al_2O_3, 5.3×10^{-6}/K for W) is closer to that of Fe-40Al (21.8×10^{-6}/K). Taking these factors into account along with the availability of fibers, Al_2O_3 was chosen for Fe-40Al.

The selection of FeCrAlY for this project was primarily based on a developmental study by Draper et al. [75] in which the viability of FeCrAlY/Al_2O_3 and FeAl/Al_2O_3 systems was investigated. From the comparison of properties in Table 2, FeCrAlY possesses a higher room temperature ductility and lower CTE than FeAl as well as a higher oxidation resistance [75,76]. The properties of FeCrAlY will be explained in more detail in the following section. The composites developed by Draper et al. were fabricated using the foil-fiber-foil method [44,45]. The fibers used were single crystal Al_2O_3 Saphikon® monofilaments (150 μm dia.). From microstructural observation, both matrices were chemically compatible although the FeCrAlY composites showed some slight reaction product after heat treatment.

Fiber pushout tests were used to determine the interfacial shear stress between the fiber and matrix. The FeCrAlY composites displayed a much higher interfacial debond strength and frictional shear strength than the FeAl composites indicating FeCrAlY/Al_2O_3

Table 2. Properties of FeCrAlY and Fe-40Al [75,76]

Matrix	Density (g/cc)	Melting pt. (°C)	CTE (10^{-6}/K)	Oxidation resistance	%elong @ RT
FeCrAlY	7.2	incipient 1357 liquidus 1482	14	1500K	4 to 12
Fe-40Al	6.1	1450	21.8	1300K	2 to 5

has a strong fiber matrix bond. The thermal properties also suggested FeCrAlY/Al_2O_3 to be more favorable. Dilatometry results indicated matrix plastic deformation in the FeCrAlY/Al_2O_3 samples relieving thermal stresses, and no cracking or debonding after thermal cycling. The FeAl/Al_2O_3 samples exhibited debonding during dilatometry measurements and large fiber displacements occurred during thermal cycling.

It is important to note that the previously cited works involved the use of large diameter fibers as reinforcements. The focus of this study is to produce fine diameter fiber reinforced composites. As discussed earlier in section 2.1, fine diameter fibers offer many advantages over large diameter fibers.

FeCrAlY Alloys

FeCrAlY alloys have been developed as a result of studies on FeCrAl alloys which have been known for excellent oxidation resistance properties [77]. This oxidation resistance is due to a surface film of Al_2O_3 formed by selective oxidation of the aluminum. However, during cyclic oxidation the oxides do not adhere well at elevated temperatures and spalling occurs upon cooling. As a result, lateral growth of the oxide develops and a complex, twisted structure is formed. Wukusick and Collins [76] have demonstrated that

by adding yttrium to FeCrAl alloys, the oxidation resistance is improved as a result of the adhesion of the surface oxides. However, the mechanism responsible was not clearly identified. Oxidation tests report the alloy to be oxidation resistant at 1533 K and still maintain a relatively good oxidation resistance at 1700K which is above the incipient melting temperature. In a further study of this phenomenon, Golightly et al. [78] concluded the addition of yttrium reduces the outward diffusion of the aluminum preventing any oxide formation within the existing oxide layer and lateral growth does not develop.

The FeCrAlY alloy is a two phase structure consisting of a body centered cubic solid solution matrix and a dispersion of an intermetallic compound, YFe_9. Despite the advantage of high temperature oxidation resistance, these alloys display low room temperature ductility and the tensile strength varies considerably with temperature [77]. Wilson et al. [79] prepared FeCrAlY alloys by mechanical alloying and reported elongations of 12% and 6% at room temperature for Fe-25Cr-6Al-2Y and Fe-25Cr-11Al-1Y (wt%) alloys respectively. These values remained constant until approximately 400 ^{o}C where ductilities rose to a maximum of 30% at 600 ^{o}C for the Fe-25Cr-6Al-2Y alloy and 40% at 800 ^{o}C for the Fe-25Cr-11Al-1Y alloy. The tensile strengths ranged from values as high as 1300 MPa at room temperature to as low as 70 MPa at 1000 ^{o}C. Wukusick [76] reported room temperature elongation values as low as 5% and tensile strengths of 540 MPa at room temperature and 20 MPa at 1000 ^{o}C for a Fe-25Cr-4Al-1Y (wt%) alloy. Although the tensile strengths differ because of the heat treatments applied, the strength decrease trend is similar and also characteristic of ferritic stainless steels [77].

FP Al_2O_3 fibers

FP alumina fibers (Dupont de Nemours) are fine diameter continuous fibers that are almost pure alpha alumina (>99%). The density is 3.95 g/cc and the average diameter is 20 μm [80]. The structure is polycrystalline. The basic fabrication process includes mixing a slurry with selected alumina particles with additives so that it is spinnable, dry spinning the fibers from the slurry, and firing the fibers to densify them [2].

The mechanical properties of the fiber indicate a tensile strength of 1380 MPa and a modulus of 380 GPa [80]. The use of the fiber is limited to 1000° C due to a decrease in strength as a result of creep [80,81]. The presence of grain boundary sliding at elevated temperatures results in creep failure.

The fibers have been successfully used as a reinforcement of light alloys, but the production did not progress beyond the plant stage and commercial production has since ceased [80]. However, it was chosen for this research project because of availability at the time and chemical compatibility with the matrix. Since the goal of this project is to produce a fine diameter fiber reinforced composite, the materials selected would provide the best choice to show the colloidal suspension process can be used to produce fiber reinforced composites.

3. EXPERIMENTAL PROCEDURE

This research project consisted of three main stages. First, the fiber coating parameters were selected based on Electrokinetic Sonic Amplitude (ESA) measurements and stability ratio calculations. Second, the fibers were coated and laid up as plys. Third, the composite plys were consolidated. Following consolidation, the composites were then characterized in terms of density, microstructure, and tensile properties.

3.1 Materials

Two different batches of prealloyed, atomized FeCrAlY powder supplied by NASA Lewis Research Center, Cleveland, OH were used in this project. Figure12 (a) shows a -325 mesh (45 μm seive opening) powder. The irregular platelike appearance of the powder is due to a prior cryomilling treatment to reduce the particle size which will enhance the matrix infiltration of the fiber tow. A -500 mesh (25 μm seive opening) powder is shown in Figure 12 (b) and has a spherical morphology. The chemical composition in atomic percent for each powder batch is shown in Table 3.

Table 3. Chemical composition of FeCrAlY powders in at%.

Powder Size	Fe	Cr	Al	Y
-325 mesh	balance	24.0	8.0	0.06
-500 mesh	balance	24.0	7.6	0.10

FP Al_2O_3 fibers, supplied by E.I. Dupont de Nemours, Wilmington, DE, were used as the reinforcement. The fibers in the as-received state are shown in Figure 13. The average filament diameter is 20 μm (± 4 μm) with an average of 60-70 filaments per tow.

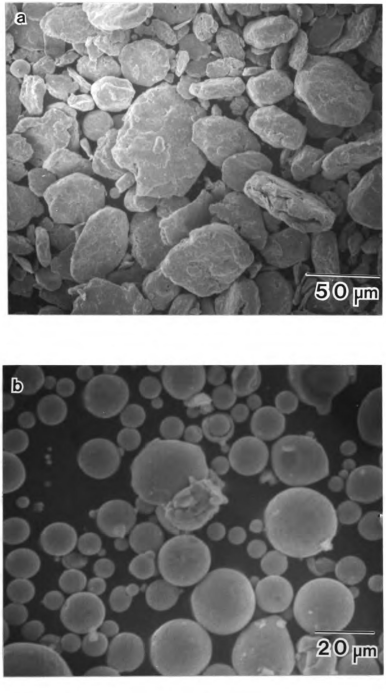

Figure 12. SEM micrographs of FeCrAlY powder batches (a) -325 mesh (45 µm seive opening) cryomilled and (b) -500 mesh (25 µm seive opening).

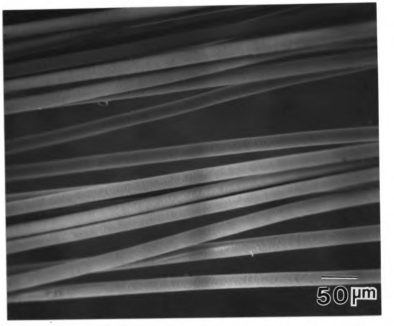

Figure 13. SEM micrograph of FP Al_2O_3 multistrand fibers.

3.2 Processing Method

ESA Data and Stability Predictions

Particle size analysis

To measure the zeta potential of the components, a particle size analysis was performed because the ESA measurement is dependent on particle size [57]. SEM micrographs were used in determining the average size of the powders. Several micrographs of the powder samples were taken at the same magnification and the particles were sized from each micrograph. This technique provided a statistical representation of the powder sample. Because of the irregular shape of the -325 mesh (45 µm seive opening) powder, an equivalent spherical diameter was calculated from the projected area of the particles [82]. An example of this technique is shown in Figure 14.

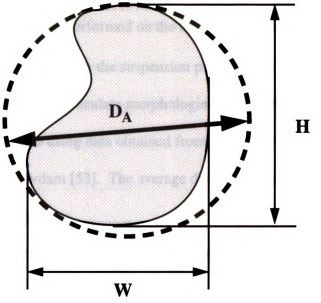

Figure 14. Projected area and equivalent spherical diameter of an irregular, rounded particle. Adapted from [82].

The equivalent spherical diameter D_A is calculated by setting the projected area A equal to the equivalent area of the circle.

$$A = \frac{\pi D_A^{\,2}}{4} \tag{3.1}$$

Rearranging,

$$D_A = \left(\frac{4A}{\pi}\right)^{\frac{1}{2}} \tag{3.2}$$

The average particle size obtained from the measurements and calculations was 32 μm ± 13.15 μm. The spherical morphology of the -500 mesh powder (25 μm seive opening) allowed the particle diameters to be measured directly from the micrographs.

The average particle size measured was 6.8 μm ± 4.4 μm.

Particle size analysis was performed on the FP Al_2O_3 fibers after they were ball milled in a methanol solution. Although the suspension process uses continuous fibers, the ESA apparatus is only set up for particulate morphologies [52,53,56]. Thus, the zeta potential measurements were made using data obtained from ground FP fibers that were used in previous research by Suydam [53]. The average diameter measured was 1.06 μm.

Zeta potential measurement

A Matec 8000 Electrokinetic Sonic Amplitude apparatus was used to perform the zeta potential measurements for each of the components. Suspensions were prepared in 250 ml solutions of 10^{-3} N KNO_3 electrolyte and contained 0.5 v/o solid for the FeCrAlY suspensions and 0.2 v/o for the FP fiber. The electrolyte concentration used was based on results of Suydam's experiments with an $FeAl/Al_2O_3$ system [53] where it was determined that the ideal electrolyte concentration for the suspension was between 0.001N and 0.0001N KNO_3. The particle parameters of each component (density and radius) were then input into the ESA program. Separate runs were conducted for each batch of FeCrAlY powder. The zeta potential was measured over a range of pH values from 2 to 10. The pH was adjusted automatically by potentiometric titrations of either HNO_3 to lower the pH, or KOH to raise the pH. Once the ESA runs of the components were completed, the results were plotted and the data from the titration points entered into a computer program, *Suspension Stability*© [56], to determine the optimum conditions to coat the fiber.

Stability Predictions

Zeta potential data from both the FP fiber and FeCrAlY powder were input into the *Suspension Stability*© program and stability ratios calculated for the composite system. The results were then plotted. This was done for both composite systems, the -325 mesh (32 μm ± 13.15 μm) FeCrAlY/Al_2O_3 and -500 mesh (6.8 μm ± 4.4 μm) FeCrAlY/Al_2O_3. From the plots, the ideal pH for maximum coating of the fibers with the matrix was chosen by identifying the values at which the matrix/fiber interaction would be unstable.

Fiber coating experiments

To provide an experimental verification of the stability ratio results, fiber coating experiments were carried out for each composite system. Suspensions of 150 ml 10^{-3} N KNO_3 electrolyte containing 25 v/o FeCrAlY powder were prepared and the pH value of the suspension was adjusted from 3-10 in increments of 0.5 using either HNO_3 or KOH. Once the pH was adjusted, the alumina fibers were fed through the FeCrAlY suspension and wound onto a teflon mandrel several times using a filament winding machine. The tows were removed from the winding machine while still wet and cut into two inch segments. Several coated tows were then placed in an alumina boat and partially sintered at 1100°C for 1 hour. Partial sintering was performed to facilitate handling of the specimens. The coated fibers are very fragile once the electrolyte has dried and any slight touch during handling results in the matrix powder falling off. After partial sintering was completed, sections from the composite were cut and mounted on aluminum stubs and the cross sections were observed in a Hitachi S-2500 SEM to provide an indication of how well the matrix infiltrated the tow.

3.3 Composite Layup Process

The layup process was carried out using a filament winding system and throughout the course of the project, modifications were made in order to make the process more efficient. The basic design will be discussed in the following subsection. The subsection describing the layup process will be divided into two parts, one part for the -325 mesh (32 μm ± 13.15 μm) powder and the other for the -500 mesh (6.8 μm ± 4.4 μm) powder. This will allow the modifications made to winding system to be shown more clearly.

Winding system design

The filament winding system, developed by Maglaya [83]and Suydam [53] is schematically shown in Figure 15 (a) and the actual system is shown in Figure 15 (b). The design is similar to that used in slurry methods for preparing long fiber reinforced ceramics [84] where the fibers are passed through a slurry containing binder and other additives and then wound onto a spool and dried. For this particular design, the fiber tow is passed from the delivery spool through a series of adjustable guide rollers. The function of these rollers is to lay down the tow and spread it as it enters the suspension bath. The rollers are positioned so that the fiber tow travels over a maximum radius of curvature which reduces the stress on the tow supplied by the tension as it passes over the rollers.

The tow is guided through the suspension by an adjustable roller unit housed in the bath as shown in Figure 16. The unique properties of the suspension allow the fibers to remain spread apart and the matrix to adhere to the fibers without the aid of a binder. A halved 1000 ml Nalgene bottle is used to hold the suspension. The semicircular area allows the tow to be coated more thoroughly because the suspension is more concentrated in the area around the tow. The roller unit shown is the current modified version.

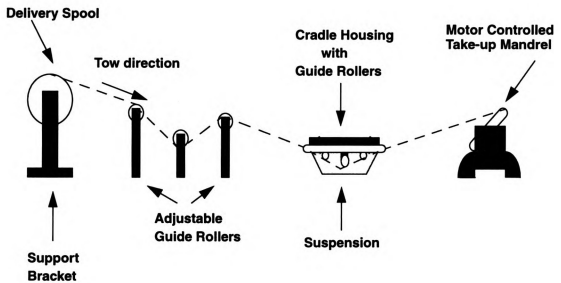

Figure 15 (a). Schematic illustration of filament winding system used to process continuous fiber reinforced MMCs.

Figure 15 (b). Photograph of winding system.

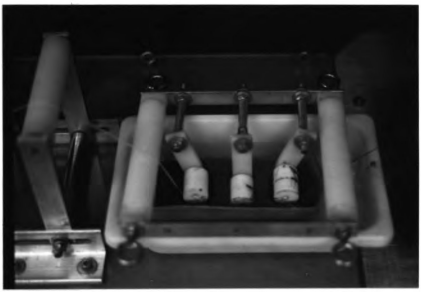

Figure 16. Photograph of suspension bath and roller unit assembly.

The center groove in the right end roller guides the coated tow onto the take-up mandrel. The mandrel is made out of virgin teflon to provide a non stick surface so a minimal amount of matrix powder is lost when removing the fibers from the mandrel.

The mandrel assembly is schematically shown in Figure 17. Two Dayton DC gear motors provide rotational and transverse movement to the mandrel. Each motor is powered by a HP E3612A DC power supply. This allows the movements to be independent of each other so more accuracy could be obtained during winding. The mandrel is mounted on a support plate attached to a base containing a threaded rod. The threaded rod allows the assembly to move in a transverse direction. Attached to the base is a switching track assembly. When the switch is activated, the polarity in the motor reverses causing the assembly to move in the opposite direction. This allows winding in both directions. The

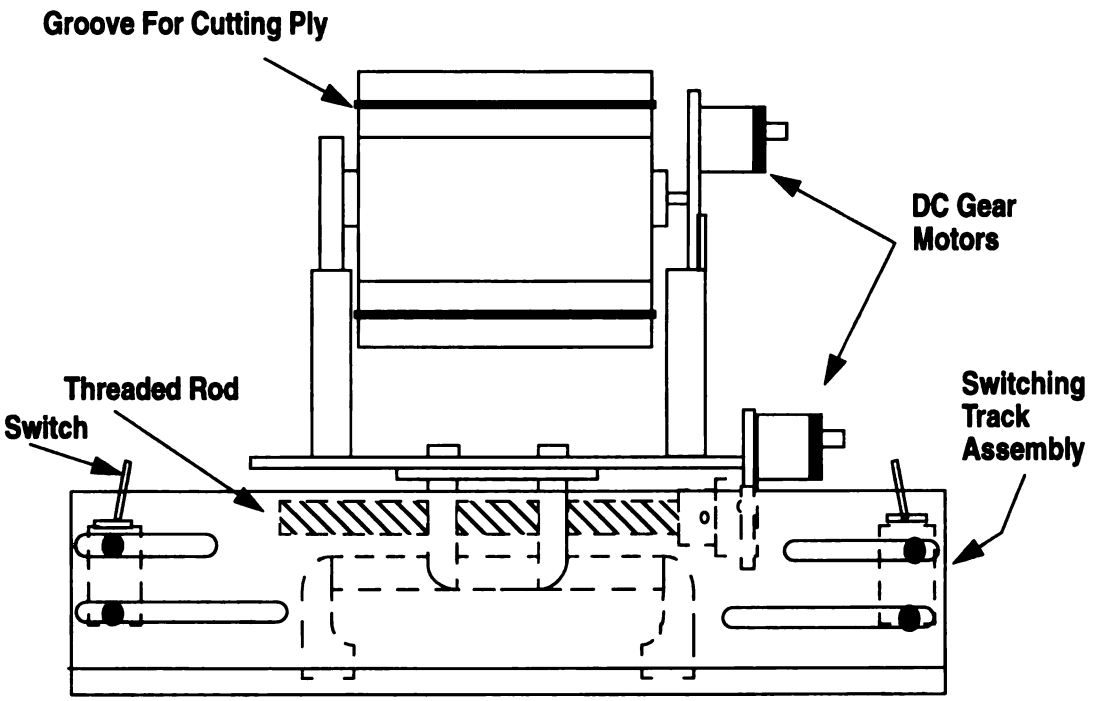

Figure 17. Schematic of mandrel assembly.

position of the switches is also adjustable. This allows plys of varying width to be fabricated. Grooves are located on the top and bottom of the teflon mandrel to allow cutting the ply and removing it from the assembly.

The design principle is similar to that of a filament winding machine used by Armstrong et al. [85] in the fabrication of W-1% ThO_2 reinforced FeCrAlY matrix composites. A threaded rod connected to the take up drum was used to laterally advance a fiber guide assembly across the rotating drum. However, the width of the ply and fiber spacing was adjusted by switching gears in the guide assembly whereas the adjustments for fiber spacing and ply width on the assembly shown in Figure 17 are made by the switch position on the track and the transverse speed of the mandrel which is controlled by

the power supply. It is important to note that the fibers used by Armstrong et al. were large diameter fibers (250 μm). The fibers used for the current research are fine diameter fibers and the spacing is more difficult to control. The features on the assembly shown in Figure 17 compensate for this and can be adapted for large diameter fibers as well.

-325 mesh (32 μm ± 13.15 μm) composite layup

A 150 ml 35 v/o FeCrAlY, 10^{-3}N KNO_3 electrolyte suspension was prepared and adjusted to pH 6 based on the results from the stability predictions and fiber coating experiments. The Al_2O_3 fibers were fed through the suspension and wound onto a mandrel using the filament winding machine shown in Figure 15. The unidirectional plys or mats were then cut from the mandrel while still wet and sectioned into the specimen sizes of 2" × 2" (50 mm × 50 mm), 2" × 6" (50 mm × 150 mm), and 2" × 8" (50 mm × 200mm). The wet mats were placed inside stainless steel rings spotwelded to molybdenum sheets. The rings provide constraint on the specimen during hot pressing to keep the matrix concentrated around the fibers and from flowing outward into the die. The sheet assemblies are schematically shown in Figure 18. The specimens also had to be cut down slightly from their original size to fit inside the area bounded by the rings. The ring thicknesses used were 3/32" (2.4 mm) for the 2" × 2" (50 mm × 50 mm) and 2" × 6" (50 mm × 150 mm) samples, and 1/8" (3.2 mm) for the 2" × 8" (50 mm × 200mm) sample. Extra suspension was spread evenly on the bottom of the assembly to provide a buffer layer to avoid excessive force on the fibers during consolidation. Also, the extra suspension can replace any matrix lost during removal of the mat from the mandrel. Once the specimens were laid in the ring assembly, additional suspension was spread on top of the mat. A molybdenum face sheet was then placed on top of the specimen and secured with a clamp. The

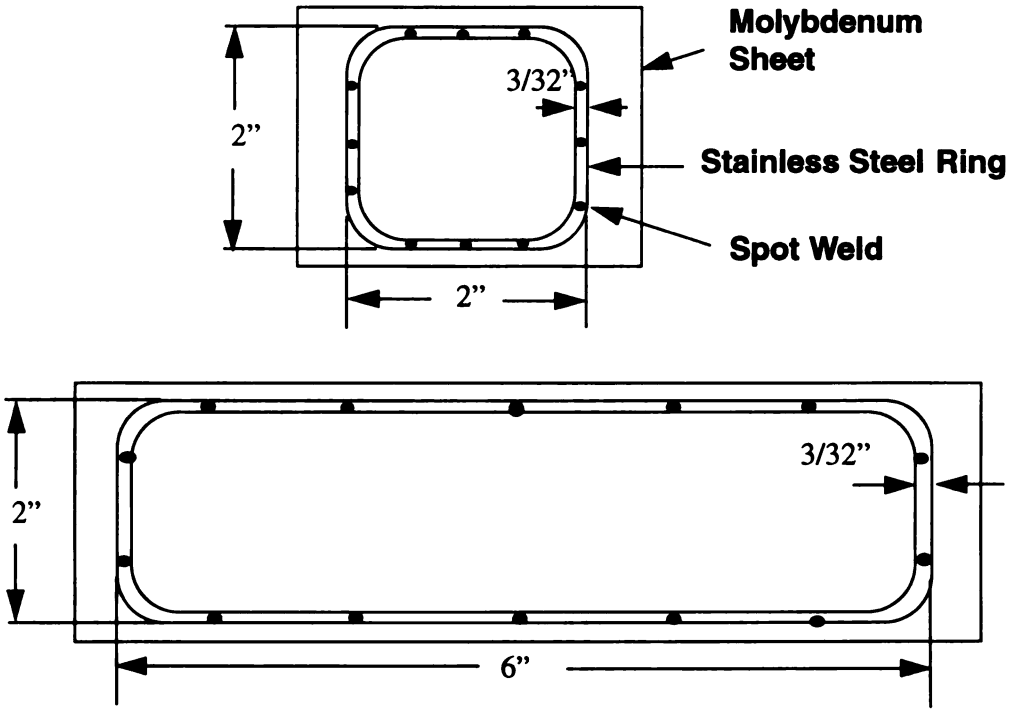

Figure 18. Schematic of the ring assemblies used in the layup process.

samples were then vacuum hot pressed.

To obtain an indication of the efficiency of the filament winding machine, an additional 2" × 6" (50 mm × 150 mm) specimen was laid up by manually coating the fibers. Tows were drawn through the suspension individually by hand and laid into the ring assembly until the area was filled.

During the layup of these composites, there was difficulty in keeping the particles in suspension. Although there was no flocculation or agglomeration of the powder in the suspension, the particles would settle and the suspension would become thicker and impede the forward motion of the tow resulting in the tow agglomerating under the roller and breaking. Thus, the suspension required agitation or stirring to keep the particles

suspended. However, the bath roller design as schematically shown in Figure 19 (a) only provided limited space to stir the suspension. The winding process had to be stopped and the roller unit removed so the suspension could be stirred. This resulted in the tow having to carefully be repositioned to resume the process. The roller unit was modified by removing part of the assembly and shortening the roller width as shown in Figure19 (b). This created additional space in the bath area and allowed the suspension to be stirred without having to stop the winding machine.

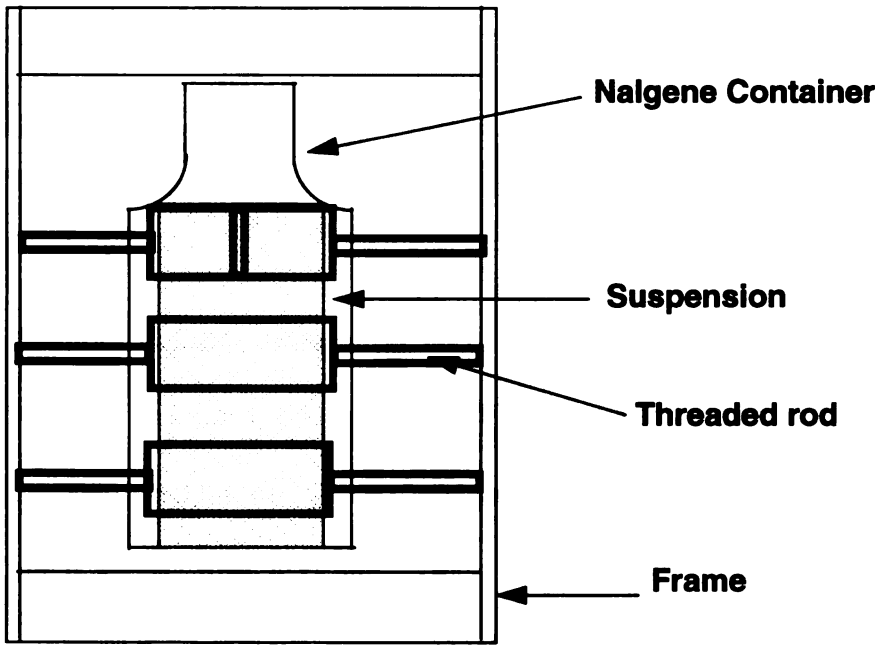

(a)

Figure 19 (a). Schematic of original roller unit.

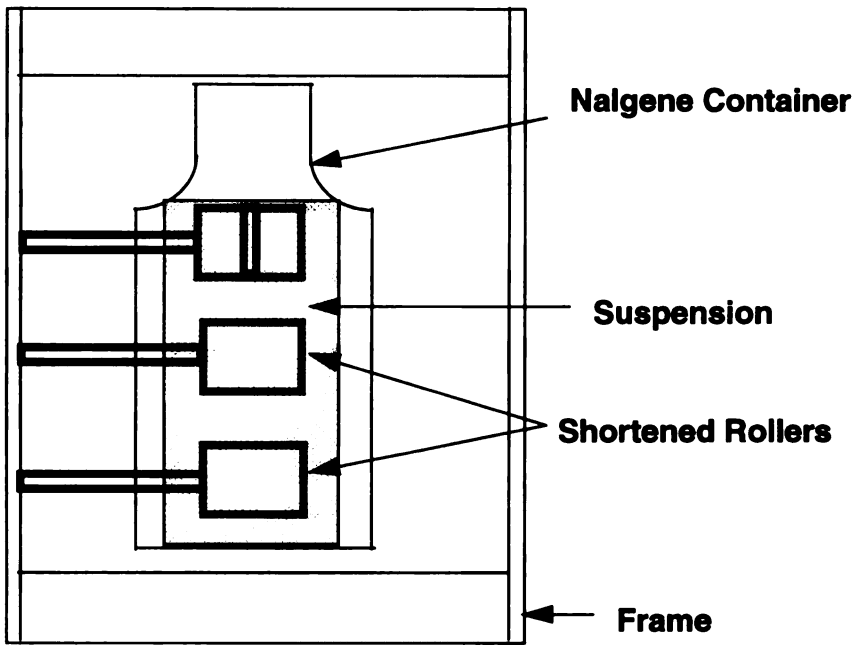

(b)

Figure 19 (b). Schematic of modified roller unit.

-500 mesh (6.8 μm ± 4.4 μm) composite layup

A -500 mesh (6.8 μm ± 4.4 μm) FeCrAlY powder suspension was prepared with the same parameters used for the -325 mesh (32 μm ± 13.15 μm) composite layup. The filament winding machine shown in Figure 15 was used to feed the Al_2O_3 fibers through the suspension and form the composite mats. The mats were then cut to the specimen size and placed in the ring assemblies for hot pressing. The specimen dimensions were 2" × 2" (50 mm × 50 mm) and 2" × 6" (50 mm × 150 mm).

For this material, problems were encountered with the positive tension from the take-up mandrel. Positive tension would break the tow, so the delivery spool was manually turned to provide some slack to keep the tow from breaking. However, it became

difficult to keep track of both the suspension and the delivery spool. To alleviate the problem, the delivery spool was modified using a belt drive system as shown if Figure 20. A rotational ball mill was used to power the assembly. A belt was attached from the rollers on the ball mill to the delivery spool to allow the spool to rotate freely and provide slack in the line. The rotational speed was slightly faster than that of the mandrel and to minimize the resulting slack, a remote switch was connected to the ball mill so it could easily be turned off and on again.

Figure 20. Modified delivery spool assembly.

Consolidation

All of the specimens were consolidated by vacuum hot pressing. This stage was carried out at NASA Lewis Research Center, Cleveland Ohio. The initial hot press parameters used for the composites were 15 ksi (103 MPa) at 1950° F (1066° C). A 2 ksi (14 MPa) clamping load was applied to the specimen until the consolidation temperature was reached. Then the consolidation pressure was applied and held at temperature for one hour. After examining the microstructure and mechanical data from a number of specimens, the hot press schedule was varied for the subsequent batch of specimens so the optimum parameters could be found that would yield a composite that was fully consolidated with minimal fiber damage. The pressures used were 7.5 ksi (52 MPa), 10 ksi (69 MPa) and 15 ksi (103 MPa) and pressing times varied from 1 hour to 1.5 hours. The pressure was also slowly ramped over a period of one hour to consolidation pressure to reduce fiber damage. The temperature was held constant at 1950° F (1066° C) because this consolidation temperature was close to the maximum use temperature of the hot press. Also, the properties of FP fibers degrade at 1000°C (1832° F) [80].

3.4 Characterization

The composites were characterized using non destructive evaluation (NDE), density measurements, optical and scanning electron microscopy, and tensile testing, to determine if the colloidal processing method used to fabricate the composites was successful in obtaining dense composites with well distributed reinforcements and improved mechanical properties.

NDE evaluation

X-Ray radiography was performed on some of the specimens to qualitatively measure any porosity or density differences, fiber damage, and alignment on a macroscopic scale [85,86]. This procedure was performed at NASA Lewis Research Center with the assistance of G. Baklini. The specimens were ground along the edges so they could be positioned flat., but it was not necessary to remove the stainless steel ring. The X-ray tube voltage used was 60 KV with a current of 0.25 mA. The object distance and exposure times were adjusted so a clear image could be obtained. The object distances used were 24 inches and 30 inches and the exposure times were 20 min., 30 min. and 40 min.

Density measurement

To quantitatively measure the density of the specimen, Archimedes' method [87] was used. The stainless steel rings were ground away so only the composite density would be measured. The specimens were weighed in air and the mass was recorded. The samples were then weighed suspended in water and the mass was recorded. The following equation was used to calculate the density:

$$\rho = \frac{M_a \rho_w - M_w \rho_a}{M_a - M_w} \tag{3.3}$$

where M refers to the mass in grams, ρ the density in g/cm^3, and the subscripts a and w refer to *air* and *water* respectively. The density values used were 1.0 g/cm^3 for water and 0.001205 g/cm^3 for air. After the densities were measured, the specimens were prepared for metallography.

Metallography and Image Analysis

The specimens were sectioned using a Beuhler Isomet low speed saw and a Struer's Accutom 5 high speed saw. The sections were cut so that both transverse and longitudinal areas could be viewed. This provides information on the distribution, volume fraction, and whether there was fiber damage. Metallography was also carried out on the longer specimens but only on limited areas because these specimens were mainly used for mechanical testing. The areas were selected so the information obtained would be a general representation of the entire specimen. Areas were also chosen based on NDE results to correlate areas of uniform and non uniform densities. Preliminary specimens were mounted and polished at NASA Lewis Research Center. All other specimens were polished at Michigan State University using the following described procedure.

The specimens were mounted in epoxy or bakelite. Specimens were placed in plastic mold cups and a 5 to 1 epoxy resin/hardener mixture was poured into the mold and the specimens were allowed to cure for 24 hours at room temperature. A LECO mounting press was used for the specimens mounted in bakelite. The specimens were placed inside the press mold and two teaspoons of bakelite powder were poured in over the specimen. The specimens were compressed at 4200 psi (29 MPa) and 285-300^{o} F (141-149^{o} C) for 5 minutes. The specimens were then removed from the press and allowed to cool.

The samples were polished using silicon carbide paper and cloth with diamond paste compound. Specimens were first ground on 120, 180, 240, 320, and 400 grit paper to remove any excess layer of epoxy or bakelite formed during mounting and to provide a rough polish. Final polishing was accomplished using 15, 9, 6, 3, and 1 μm diamond paste and a Metaserv mechanical polisher.

Optical microscopy was carried out using a LECO Olympus benchtop metallograph. Both the transverse and longitudinal sections of the samples were examined and micrographs were taken using Polaroid 55 film to record the observations. After viewing some of the longitudinal areas, it was noted that there was some porosity. However, this was not apparent on the transverse areas. To determine if the porosity lies only on or near the surface, 50 to 75 μm of material was removed from the surface of the longitudinal area by grinding with silicon carbide paper. The specimens were then polished, viewed under the optical microscope and micrographs were taken.

The volume fraction of fiber in the composite could not be determined prior to processing because of the nature of the continuous process. From the Archimedes' measurements, a volume fraction could be calculated. However, if the sample contained porosity, the value calculated would be invalid because of the porosity making the volume fraction of fiber appear higher. To obtain a more accurate measurement of the fiber volume fraction, A LECO Neophyte optical microscope and LECO 2001 image analysis software were used. Transverse areas of the samples were viewed and field measurements were taken throughout the specimen so the volume fraction of the entire plate could be determined. The number of field measurements varied between 20 and 60 depending on the size of the specimen. A histogram was then plotted for each specimen to show the mean and standard deviation of the fiber volume fraction, The results obtained were correlated with those from the density measurements and the amount of porosity was determined.

Mechanical Testing

To determine the mechanical properties of the composite, tensile testing was performed at room and elevated temperatures. The tests were performed at NASA Lewis Research Center. Dogbone specimens were cut from 2" × 6" (50 mm × 150 mm) and 2" × 8" (50 mm × 200 mm) plates using a water jet cutter. The tensile bar design and dimensions are shown in Figure 21. An Instron Series IX Automated Materials Testing System was used to test the specimens. A full scale load range of 2,000 lbs and a cross-head speed of 0.005 in/min were used as the machine parameters. The sample parameters used were a 0.5" (12.5 mm) gauge length, a 0.25" (6.35 mm) gauge width, and a grip distance of 3.5" (88.9mm). The thickness was entered as measured. After room temperature testing was completed, elevated temperature testing was conducted at 700 K (427°C) and 1100 K (827°C).

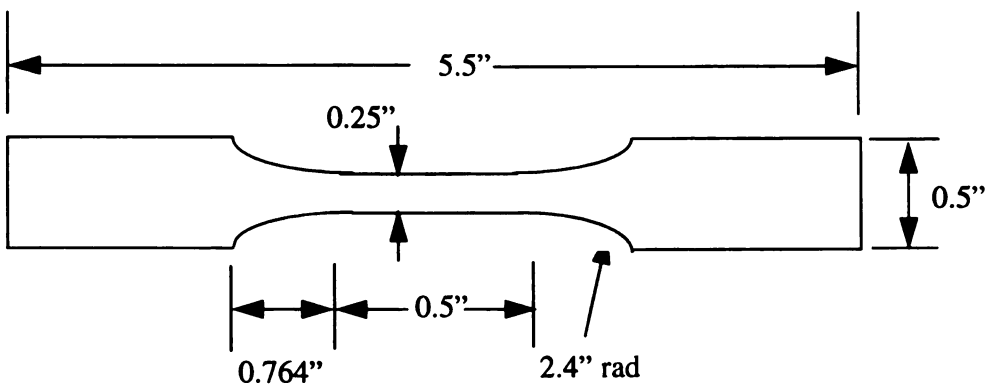

Figure 21. Schematic of tensile bar design.

Scanning Electron Microscopy

Fracture surfaces from the tensile specimens were examined using a Hitachi S-2500 scanning electron microscope. A thin layer of gold coating was applied to the specimens to eliminate charging effects from the fibers. The fracture areas were viewed to determine the type of fracture, i.e. ductile or brittle failure of the matrix, and whether or not the fibers were weakly or strongly bonded to the matrix.

4. RESULTS AND DISCUSSION

The results of this investigation will be presented as follows: the zeta potential data, stability predictions, and the results of the fiber coating experiments for both powder types will be grouped together. The processing parameters predicted were the same for both powder types and the coating experiments yielded similar results. The microstructure and mechanical testing results for the consolidated samples will be grouped according to matrix powder size.

4.1 Suspension Process Parameters

Zeta Potential

The zeta potential values for the both matrix powders and alumina fiber are plotted versus pH in Figure 22. The zeta potential for the -325 mesh (32 μm ± 13.15 μm) powder increased in magnitude from 40mV at pH 3 to 80 mV at pH 10. The zeta potential for the -500 mesh (6.8 μm ± 4.4 μm) powder gradually increased from 22 mV at pH 2 to33 mV at pH 10. Although the trends of the curves are similar, the magnitude of the zeta potentials are significantly different as well as the distribution of data points. The difference in zeta potential value was due to the difference in the particle size of the powder. Larger particles may have a higher zeta potential value because the ESA measurement is dependent on the particle size input [57]. The ESA uses an inertial correction to the dynamic mobility the particle. This factor is inversely proportional to the particle radius. A larger radius input would underestimate the inertial contribution of the correction factor resulting in a larger zeta potential value [57]. The variation in data points on the -325 mesh (32 μm ± 13.15 μm) curve is a result of the wide size distribution of the powder and particles agglomerating or settling out during measurement. The density of the powder (7.2 g/cc) is much

larger than that of powders commonly used in this type of measurement such as SiC and Si_3N_4. This effect has also been seen in results of $FeAl/Al_2O_3$ experiments by Suydam [53] and Wilson et al. [52].

The data for the ground Al_2O_3 fiber shows a curve where the zeta potential gradually decreases as the pH increases [54]. At pH 8.5, the curve reaches 0 mV. This point is referred to as the iso-electric point and represents a zero net potential on the particle's surface.

Stability Predictions

The zeta potential results were input into the computer program, Suspension Stability©, and the calculated stability plots are shown in Figures 23 and 24. Figure 23 shows the stability curve for the composite system containing the -325 mesh (32 μm ± 13.15 μm) FeCrAlY powder. The FeCrAlY is predicted to be stable or dispersed throughout the pH range because the log (W) value is greater than 10. Using this criteria to indicate stability, the Al_2O_3 fibers are predicted to be stable with respect to themselves at pHs less than 7.5. The $FeCrAlY/Al_2O_3$ interaction is unstable at pHs greater than or equal to 8, thus the FeCrAlY should coat the fibers at those pHs. Since the fibers become unstable at pHs greater than 7.5, it would appear the optimum coating conditions are near pH 7.5. This would allow the fibers to remain separated from themselves so the powder could infiltrate the tows.

The curves for the -500 mesh (6.8 μm ± 4.4 μm) composite system in Figure 24 are similar to those shown in Figure 23. The Al_2O_3 remains stable at pHs less than 7.5. The FeCrAlY powder, however, is unstable and forms agglomerates until approximately pH 8 where Log (W) gradually increases and becomes stable.

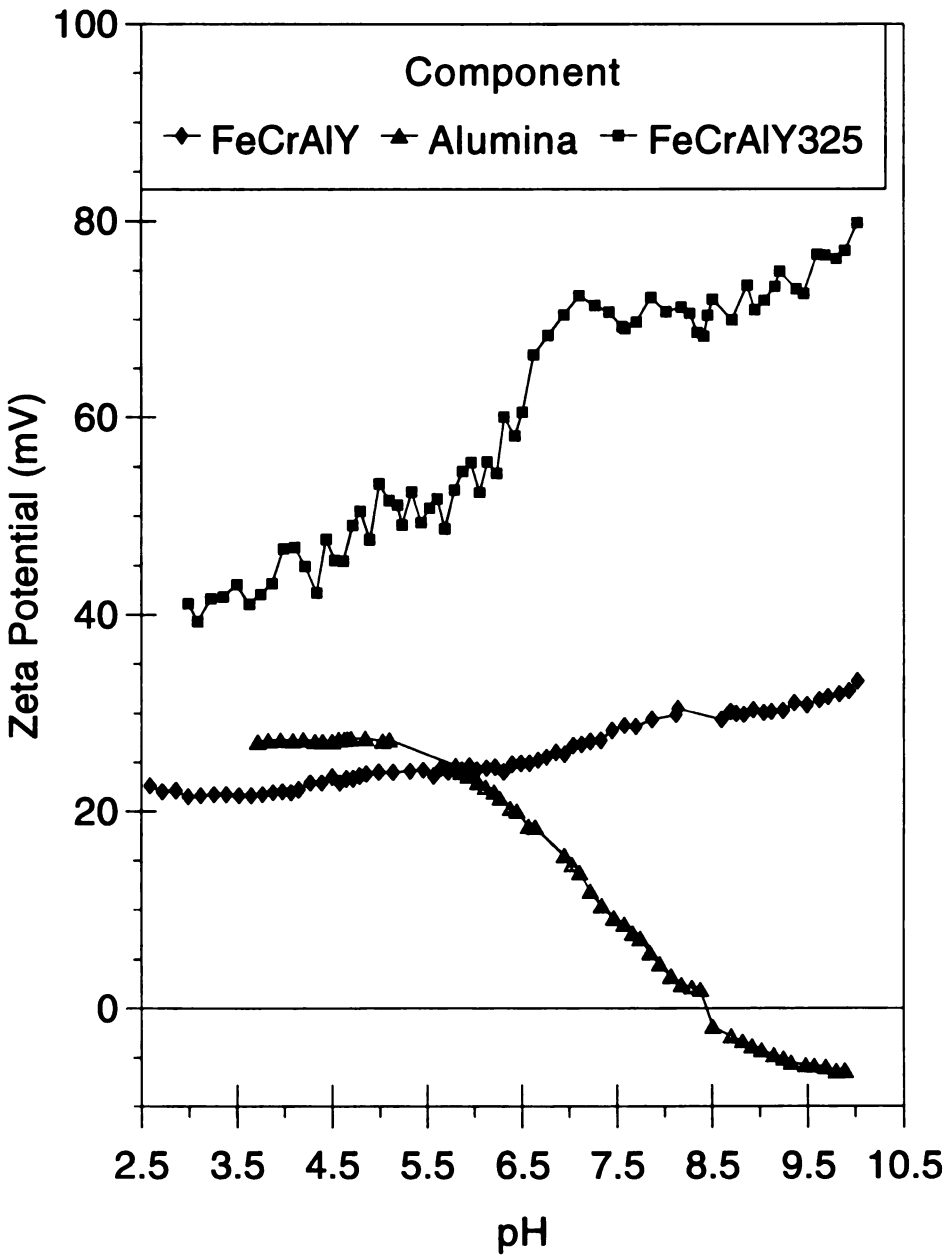

Figure 22. ESA zeta potential measurements for FeCrAlY powders and Al_2O_3 [53,89].

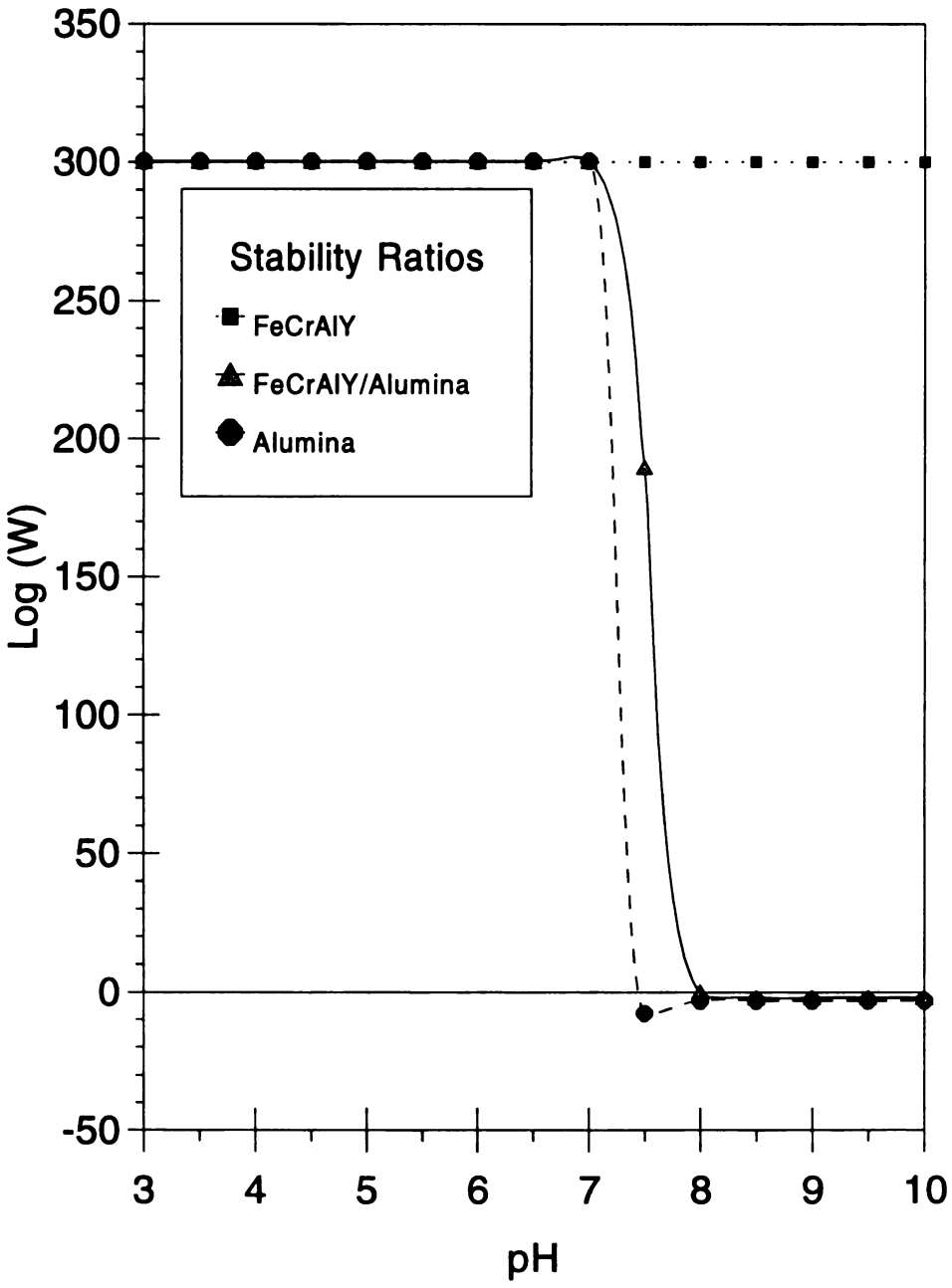

Figure 23. Predicted stability of -325 mesh FeCrAlY/Al_2O_3 system [53,89].

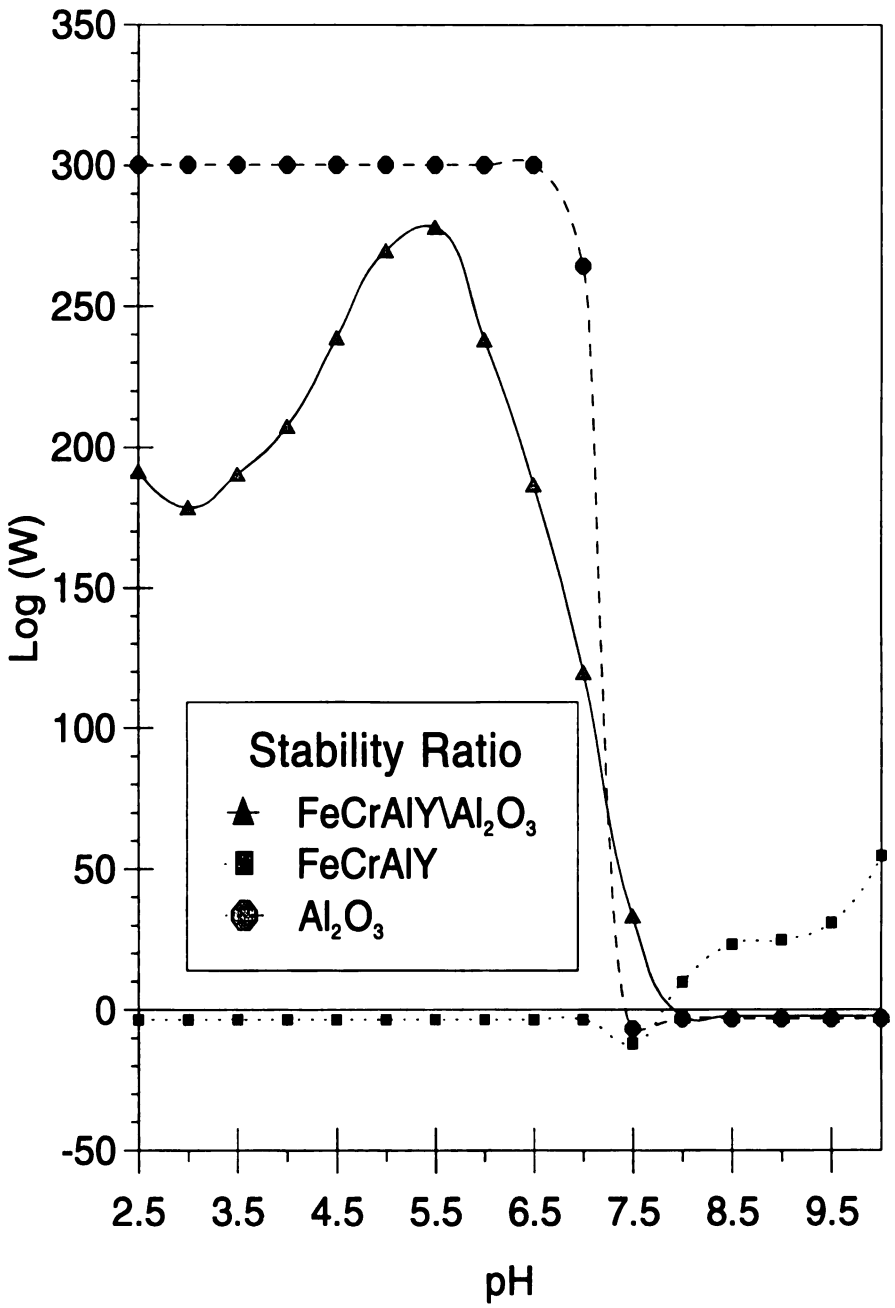

Figure 24.Predicted stability of -500 mesh FeCrAlY/Al_2O_3 system [53, 89].

The reason for this behavior is not understood. Sedimentation experiments were conducted where suspensions of FeCrAlY powder were allowed to settle at various pHs. The tests confirmed the stability behavior of the powder [89]. It is believed that the changes in stability behavior are attributed to differences in particle size and size distribution. The FeCrAlY/Al_2O_3 interaction predicts that fiber coating or heterocoagulation should occur at pHs greater than approximately 7.5. Once again, the optimum conditions were predicted to be near pH 7.5 because the fibers remained separated from themselves.

Fiber Coating Experiments

The optimum coating conditions were experimentally determined to be at pH 6. Figures 25 and 26 are SEM micrographs of partially sintered composite sections. Figure 25 shows a partially sintered composite section made using the -325 mesh (32 μm ± 13.15 μm) powder. The fibers are separated from each other and the powder has infiltrated the tows. In Figure 25, the outer fibers do not show any coating on them. This was due to handling during specimen preparation for SEM observation. However, this does allow one to see the infiltration by the matrix.

Figure 26 shows a composite section made with -500 mesh (6.8 μm ± 4.4 μm) FeCrAlY powder. The smaller particle size shows better infiltration of the tow than the coarser -325 mesh (32 μm ± 13.15 μm) powder. In addition, the spherical morphology provides a more uniform coating because the particle packing is closer than the irregular, platelike -325 mesh (32 μm ± 13.15 μm) powder.

It is also apparent from Figures 25 and 26 that there are no crevices or areas within the tow that are particle free. This is attributed to the attractive forces present on the particle and fiber and also to the winding system providing tension and squeezing the tow together

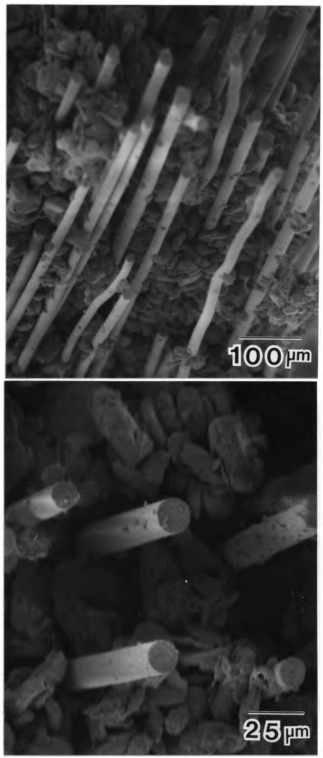

Figure 25. Partially sintered-325 mesh FeCrAlY/Al_2O_3 composite processed under optimum conditions at pH 6 showing infiltration of the tows and coating of the fibers.

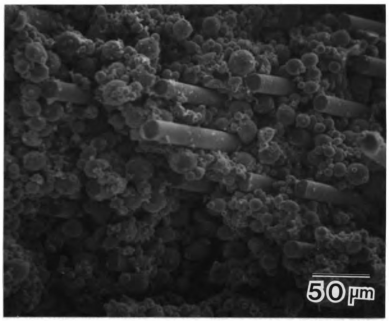

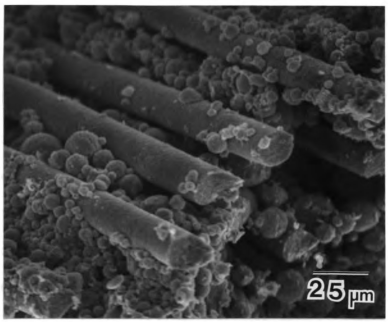

Figure 26. Partially sintered -500 mesh FeCrAlY/Al_2O_3 composite processed under optimum conditions at pH 6 showing infiltration of the tows and coating of the fibers.

when it is removed from the suspension and wound onto the take up mandrel.

Analysis of the stability predictions show the FeCrAlY powder to be stable at pH 6 for the -325 mesh (32 μm ± 13.15 μm) powder (Figure 23) and flocculation to occur at pH 6 for the -500 mesh (6.8 μm ± 4.4 μm) powder (Figure 24). It is not known whether or not the powders are flocculated as predicted because the powders' state of stability cannot be determined conclusively from Figures 25 and 26. This would require further research [89].

Suspensions were prepared at pHs 3 and 8.5 and the fibers were drawn though the suspensions to show that the coating process is due to maximizing the colloidal attractive forces between the fiber and matrix and not due to surface tension effects. The results are shown in Figures 27 and 28 for pH 3 and pH 8.5 respectively. It is apparent that the particles do not coat the fiber at these pHs. Heterocoagulation between the fiber and matrix was not predicted to occur in the low pH range for both systems. At pHs greater than 7.5 the Al_2O_3 fibers are unstable and clump together. Thus, the matrix is prevented from thoroughly infiltrating the fiber bundle.

The experimental results are in agreement with some aspects of the stability predictions. However, there is a discrepancy between the optimum experimental conditions and the predicted stability. For both systems, the optimum pH was predicted near 7.5 because that is where heterocoagulation would be maximized yet the experimental results showed the optimum conditions to be at pH 6. The reasons for this are not conclusive at this time, but some understanding can be gained by examining the micrographs of the FeCrAlY powders in Figure 12. The average particle sizes were determined to be approximately 7 μm for the -500 mesh (6.8 μm ± 4.4 μm) powder and 33 μm for the -325 mesh

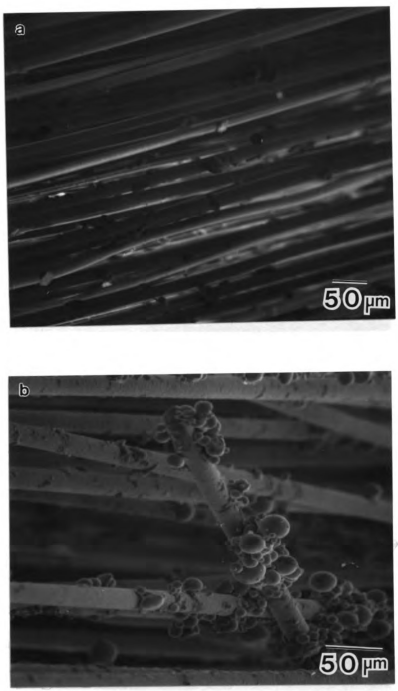

Figure 27. Partially sintered FeCrAlY composites processed under non-optimum conditions at pH3 for (a) -325 mesh powder and (b) -500 mesh powder.

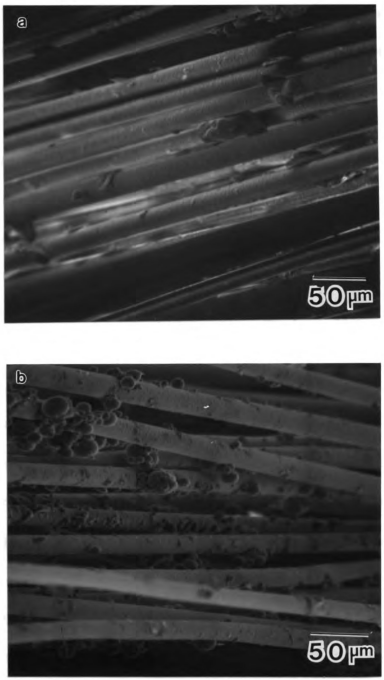

Figure 28. Partially sintered FeCrAlY composites processed under non-optimum conditions at pH8.5 for (a) -325 mesh powder and (b) -500 mesh powder.

(32 μm ± 13.15 μm) powder. During processing, the larger particles settle out of the suspension and do not participate in the coating. The ESA measurements are dependent upon the particle size and particle size is also an input parameter for the stability calculations. As a result, it is probable that shifts toward lower pHs between stability and instability occur [89].

4.2 Consolidated Specimens, -325 mesh Matrix Powder

These results will be divided into three subsections. The first two sections will discuss the NDE and microstructural results for the specimens made by manually coating the fibers and specimens made using the filament winding machine. The third section will combine the tensile test results and fracture surfaces from both types of composites because only four tests were run.

Specimens Laid Up By Manually Coating the Fibers

NDE results

The X-ray radiograph in Figure 29 shows a longitudinal view of a 2″ × 6″ (50 mm × 150 mm) specimen laid up by manually coating the fibers. The hot press parameters used were 1950° F (1066° C) at 15 ksi (103 MPa) for one hour. The arrows pointing to the light areas on the specimen indicate regions of nonuniformity. The average thickness measured was 0.94 mm ± 0.03 mm. Thickness measurements showed these lighter areas to be thinner than the other or darker regions. This was a result of the uneven placements of extra suspension above and below the ply during the lay up. It was observed during the fiber coating that some tows contained more coating than others. This is believed to be due to the variation in which the tows were drawn through the suspension as a result of the manual process. Tows were drawn through one at a time and placed into the ring assembly.

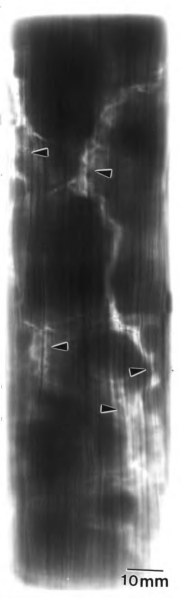

Figure 29. X-ray radiograph of FeCrAlY/Al_2O_3 specimen laid up by manually coating the fibers.

The fiber alignment is not uniform, exhibiting some wavy areas. The non-uniform alignment is attributed to the manual process. From Figure 29, it cannot be determined whether fiber damage occurred during processing. The fibers are too fine to examine with the naked eye. Microscopic evaluation of the specimen would provide a better view.

Microstructure

A transverse section of the composite is shown in Figure 30. The micrograph represents areas of the darker regions near the top and bottom of Figure 29. The middle section of the sample was used to make a specimen for tensile testing because it appeared most dense. The composite section shown in Figure 30 appears to be fully dense. The fiber volume fraction of the specimen is low, approximately 8%. The fiber distribution is not uniform and there are some areas on the micrographs where groups of fibers are touching which are indicated by the arrows. An SEM micrograph in Figure 31 shows these areas to contain small pores and within the pore, unconsolidated particles. However, the areas which have these defects are very few with respect to the whole specimen. Longitudinal sections are shown in Figure 32 (a) and 32 (b). Figure 32 (a) shows the fiber alignment is mostly straight with some slight waves. Figure 32 (b) shows a different section with a few fiber breaks.

A micrograph representing the white areas in Figure 29 is shown enlarged in Figure 33. Porosity is evident in this transverse section indicating the NDE is a valuable aid in locating problem areas within the specimen. SEM was used to provide a clearer picture of the porosity. Longitudinal sections are shown in Figures 34 (a) and 34 (b). Figure 34 (a) shows a wavy fiber alignment and porosity along the fiber and within the matrix. Figure 34 (b) is an enlarged area near the fibers. These porous areas are of concern because the

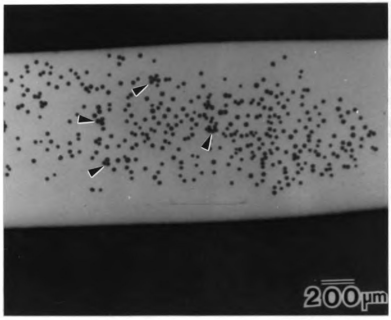

Figure 30. Transverse section of the 2″ × 6″ (50 mm × 150 mm) FeCrAlY/Al_2O_3 composite fabricated by manually coating the fibers. Arrows indicate where fibers are touching.

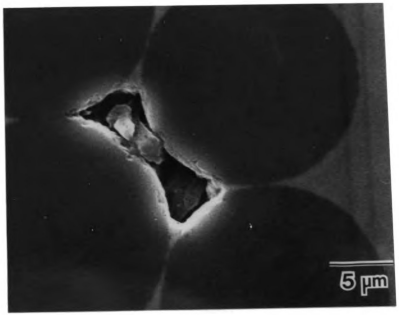

Figure 31. SEM micrograph of the 2″ × 6″ (50 mm × 150 mm) composite. The area shown is an enlarged area representative of where fibers are touching in Figure 30. These areas contain small pores and unconsolidated particles.

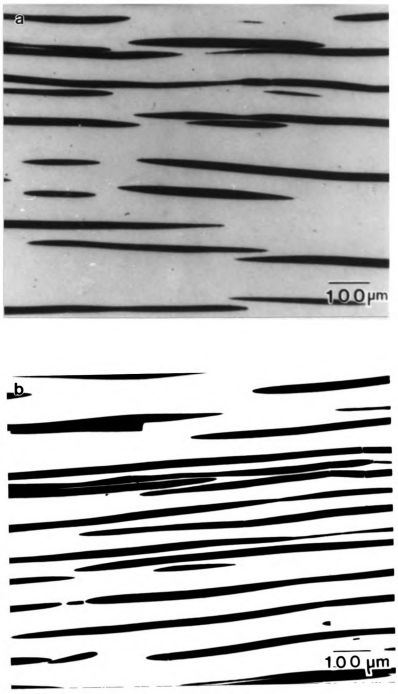

Figure 32. Longitudinal sections of the 2″ × 6″ (50 mm × 150 mm) FeCrAlY/Al_2O_3 composite laid up by manually coating the fibers showing aligned, undamaged fibers with slight waves (a), and (b), a region containing a few fiber breaks.

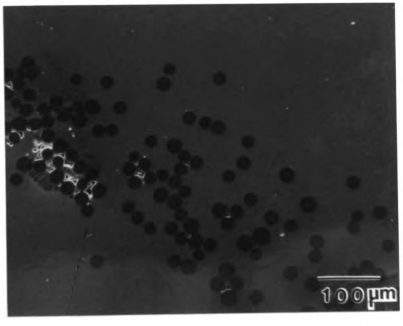

Figure 33. SEM micrograph of a transverse area from the 2″ × 6″ (50 mm × 150 mm) FeCrAlY/Al_2O_3 composite laid up by manually coating the fibers showing porosity.

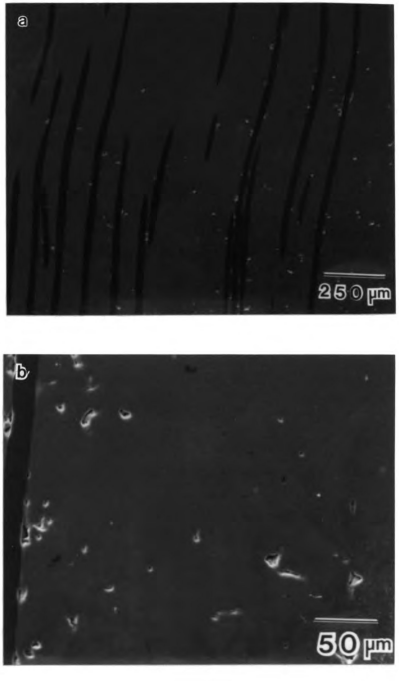

Figure 34. SEM micrographs of a longitudinal section from the 2″ × 6″ (50 mm × 150 mm) composite showing porosity and wavy alignment in (a) and (b) is an enlarged area near the fibers showing porosity.

elastic modulus, fatigue and fracture toughness are dependent on the density [82]. For this specimen, the porosity was limited to certain regions. Fiber damage was not apparent in the regions examined and could be attributed to the low volume fraction of fiber present.

Volume Fraction and Density

The average fiber volume fraction measured using image analysis was approximately 8%. Figure 35 shows a histogram obtained from the measurement. The plot shows the number of counts vs. the volume fraction of fiber. The x-axis represents the fiber volume fraction. The left y-axis represents the number of times a specific volume fraction was read. The right y-axis is the percentage of counts out of the total number of measurements which was 20. The number of measurements varied according to the specimen size that was mounted. From the mean value of fiber volume fraction, a composite density of 6.94 g/cc was calculated using the Rule of Mixtures [1]. The density value obtained from the Archimedes method was 6.86 g/cc and the difference is attributed to the porosity present. The amount of porosity determined was approximately 1.2%

There is a slight error involved in the density measurement. The Archimedes measurement showed some instability in the measurement of the sample when it was weighed in water. The scale used was very sensitive to vibration and the decimal in the thousandths place tended to drift. The difference caused a change in the final density by a few hundredths of a g/cc. The image analyzer also added some error in areas where fibers were clumped or pores were connected to fibers because the image analyzer measures the contrast differences and if the pores are connected to the fibers or in between clumps of fibers, the image analyzer measures it as a whole. The error was minimal for this specimen because of the low volume fraction of 8%.

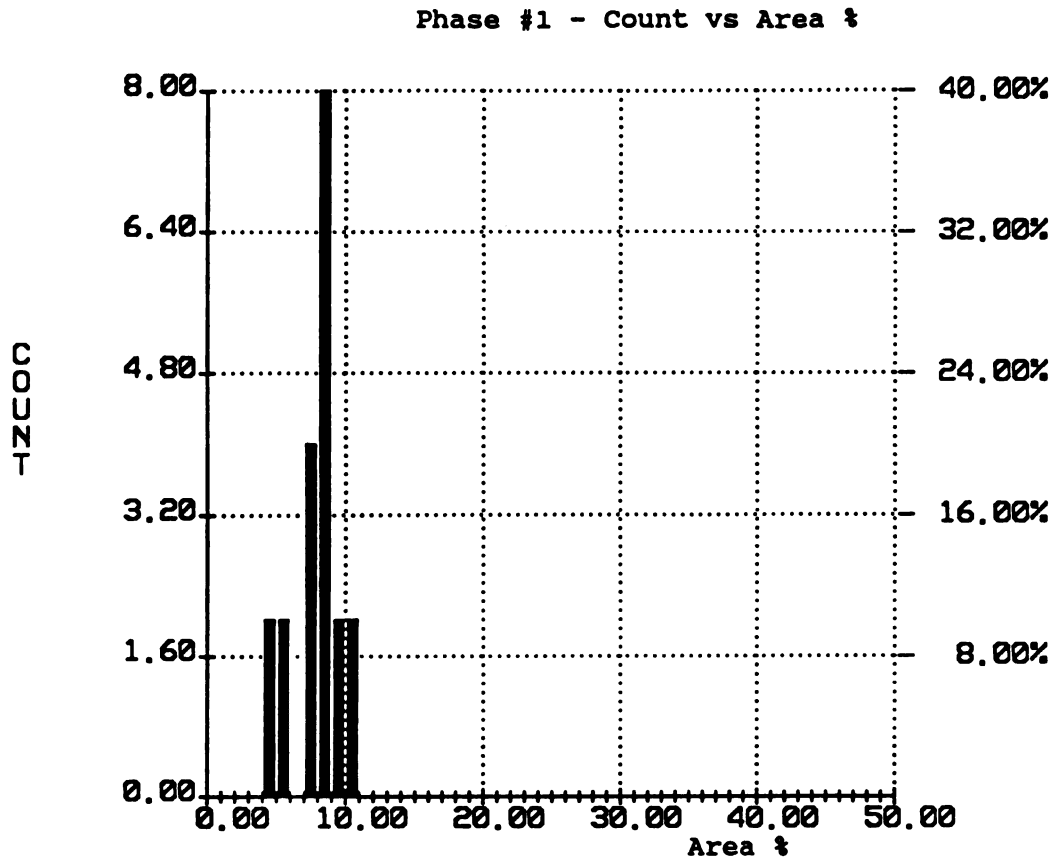

Average	:	7.977
Standard Deviation	:	1.641
Fields analyzed	:	20
Field area	:	1.639e+06 mic^2
Total area surveyed	:	3.278e+07 mic^2

Figure 35. Histogram showing the fiber volume fraction of the 2″ × 6″ (50 mm × 150 mm) composite laid up by manually coating the fibers.

Specimens Laid Up Using Filament Winding Machine

NDE results

The X-ray radiographs in Figures 36 (a), 36 (b), and 36 (c) show a longitudinal view of a 2″ × 2″ (50 mm × 50 mm) plate (a), 2″ × 6″ (50 mm × 150 mm) plate (b), and a 2″ × 8″ (50 mm × 200 mm) plate (c). Different dimensions were used to see if any consistency could be maintained between the lay-up and the microstructure. The hot press parameters used for all of the specimens were 1950° F (1063° C) at 15 ksi (103 MPa) for one hour. The average thicknesses were 0.91 mm ± 0.03 mm for the 2″ × 2″ (50 mm × 50 mm) specimen, 0.97 mm ± 0.05 mm for the 2″ × 6″ (50 mm × 150 mm) specimen, and 1.9 mm ± 0.05 mm for the 2″ × 8″ (50 mm × 200 mm) specimen. Although thickness variations were still present, the specimens appeared to be more dense than the manually laid up specimen with the exception of the center region in Figure 37 (b). Problems still existed with the placement of extra suspension above and below the ply because that was done manually and there was an inconsistency in that stage of the process.

The fiber alignment was slightly improved using the winding process. Laying up the ply in the ring assembly as a whole ply instead of one tow at a time allowed more control. However, as the specimen size increased, the harder it became to lay the ply into the ring assembly. The difficulty in the lay-up does not reflect problems with the powder size or winding. It is a handling problem.

Microstructure

The microstructure of the 2″ × 2″ (50 mm × 50 mm) plate (a), 2″ × 6″ (50 mm × 150 mm) plate are shown in Figures 37 (a) and 37 (b). The fiber volume fraction of both plates is increased to approximately 10% and the fiber distribution is improved. There are

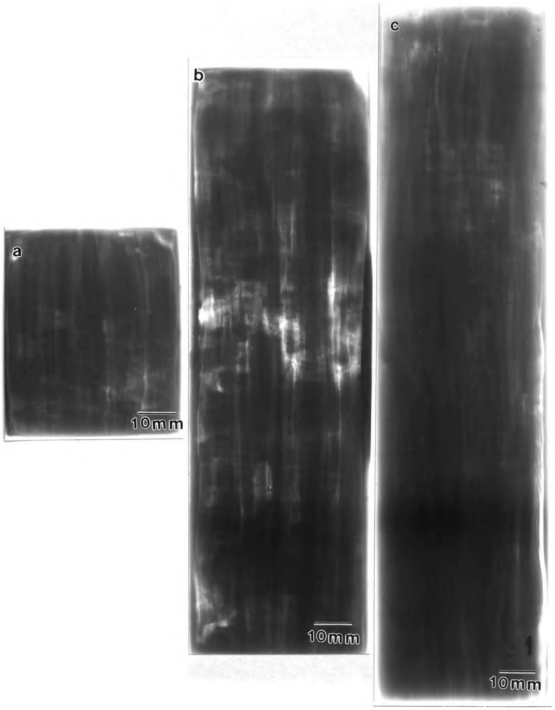

Figure 36. X-Ray radiographs of specimens (a) $2'' \times 2''$ (50 mm × 50 mm), (b) $2'' \times 6''$ (50 mm × 150 mm), and (c) $2'' \times 8''$ (50 mm × 200 mm) fabricated using the filament winding system.

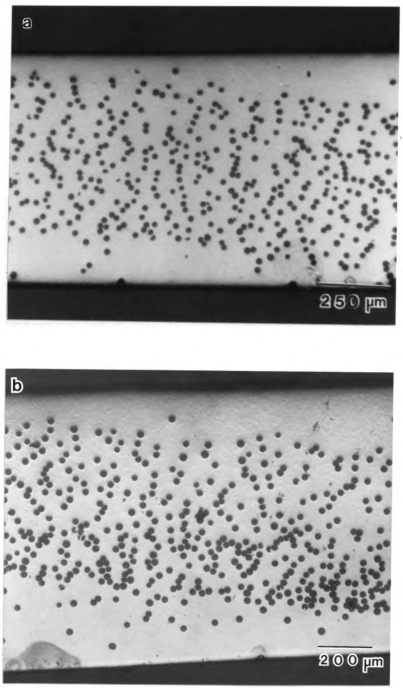

Figure 37. Transverse sections of the 2″ × 2″ (50 mm × 50 mm) plate (a) and the 2″ × 6″ (50 mm × 150 mm) plate (b) fabricated using the filament winding machine. Volume fraction is approximately 10%.

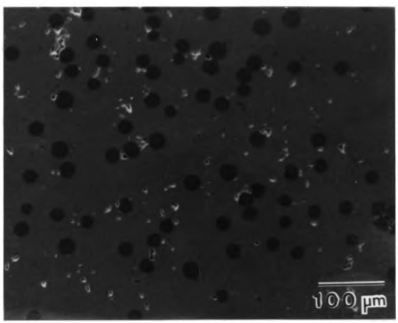

Figure 38. Transverse portion of center region in the 2″ × 6″ (50 mm × 150 mm) plate showing porosity.

also fewer regions of fiber clumping. Both sections from the plates appear fully dense. Figure 38 shows a portion of the center region of the 2″ × 6″ (50 mm × 150 mm) plate. The extent of the porosity was not known because most of the specimen was used to machine tensile bars. A possible reason for the porosity is due to the uneven suspension above and below the ply, uneven pressure application throughout the specimen and void creation. The gradient which exists may be too high for the flow of the matrix to compensate for, especially in areas where fibers are spaced closer together. There was concern about the mechanical behavior of the tensile bars from this region. One of the bars was HIPed to see if the pores could be removed. The parameters used were the same as those for the VHP.

For the 2″ × 8″ (50 mm × 200 mm) plate, an optical micrograph of the transverse section is shown in Figure 39. The fiber volume fraction increased to approximately 13%. The fiber distribution is similar to that of the other samples and the specimen appears fully consolidated.

Figure 40 (a) and 40 (b) represent the longitudinal views of the specimen. The observations were similar for all three specimens. Figure 40 (a) was taken from the 2″ × 8″ (50 mm × 200 mm) plate and Figure 40 (b). was taken from the 2″ × 6″ (50 mm × 150 mm) plate. The plates contained regions of straight and undamaged fibers such those seen in Figure 40 (a), and regions of damaged or fragmented fibers in Figure 40 (b).

The damaged fibers are of concern because fragmented fibers cannot provide effective reinforcement because the fibers would not be able to carry their portion of the load and stress concentrations would be created in adjacent fibers which could lead to premature failure [31]. In figure 40 (b), the broken fibers are aligned and there is matrix between the

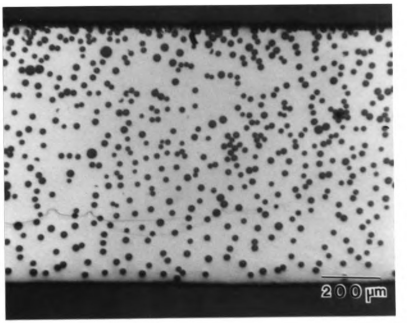

Figure 39. Transverse section of a 2″ × 8″ (50 mm × 200 mm). Fiber Volume fraction is approximately 13%.

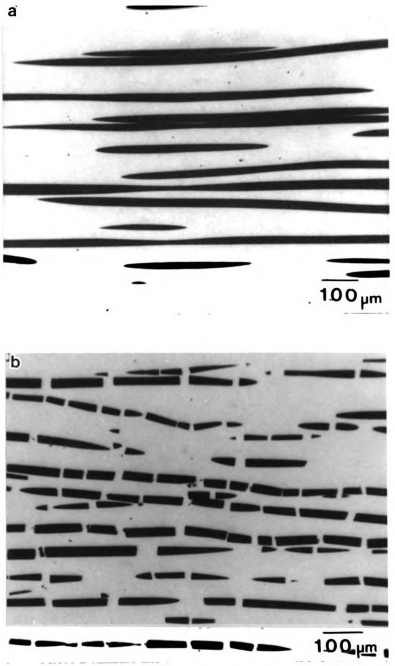

Figure 40. Longitudinal sections representing specimens fabricated using the filament winding machine. (a) shows aligned and undamaged fibers from the 2″ × 8″ (50 mm × 200 mm) plate and (b) shows aligned and damaged fibers from the 2″ × 6″ (50 mm × 150 mm) plate.

fibers indicating the fragmentation could be a result of pressure. Fiber breakage also occurs during the lay up process, but the segments are much longer and random. There was also concern that the fibers could have been damaged when the face sheet was clamped to the ring assembly to hold the composite in place for transport. The broken regions tended to extend from where the clamp was placed. Referring to Figure 36, the clamps stretched from the edge of the specimens to the center length wise. One clamp was used for each side. The clamps were placed on the sides and the ends. Micrographs were taken from areas near the clamp and away from it depending on what part of the sample was not machined for tensile testing. It was decided for the next batch of specimens that rubber bands would be used instead of clamps to avoid fiber damage.

A direct correlation between the micrograph in Figure 40 (b) and the critical length necessary for full load transfer could not be made because the interfacial shear strength data was not available for this particular composite. However, an estimate was made using interfacial shear strength data from fiber pushout tests for a FeCrAlY/Al_2O_3 composite reinforced with Saphikon© fibers [90]. The expression for the critical length (l_c) is:

$$l_c = \frac{d\sigma_{fu}}{2\tau_i} \tag{4.1}$$

where σ_{fu} is the ultimate fiber strength, d the fiber diameter, and τ_i the interfacial shear strength [1, 10, 11].

The average fiber length measured from the segments in Figure 40 (b) was approximately 87 $\pm$ 40 μm. Only the segments which had both ends square were measured

because it could not be determined whether the fragments with conical ends were portions of longer segments. Using the ultimate strength value and diameter of FP Al_2O_3 fibers (1380 MPa, 20 μm), and an interfacial shear strength value of 191 ± 18 MPa, the critical length was calculated to be approximately 73 ± 7 μm. This suggests that the fibers can still be loaded to their maximum strength except for those with segments less than approximately 66 μm. However, this estimate does not take into account the frictional shear stresses involved. The surface of Saphikon© fibers are smooth and result in a frictional shear stress value of 111 ± 11 MPa. FP fibers have a rough surface [80] and it is expected that the frictional shear stress of FP fibers is higher and could possibly influence the interfacial shear strength enough to reduce the critical length so all of the fibers can achieve their full load (even the shortest fibers in the 87 ± 40 μm range). Thus, it appears that the fiber damage shown in Figure 40 (b) may not be detrimental to the mechanical properties. It will be shown that this is consistent with the lack of fiber pullout observed on the fracture surfaces (see sections entitled *Mechanical Testing*).

Volume Fraction and Density

The histogram in Figure 41 represents the 2″ × 2″ (50 mm × 50 mm) plate and dense regions from the 2″ × 6″ (50 mm × 150 mm) plate. The density calculated from the histogram was 6.86 g/cc. The density measurement yielded a value of 6.75 g/cc. The amount of porosity was approximately 1.6%.

Figure 42 shows the mean volume fraction obtained from the 2″ × 8″ (50 mm × 150 mm) plate to be approximately 13%. The density calculated was 6.77 g/cc and the density measured was 6.70 g/cc. The difference was 1%. The error involved in the measurement of these samples was very small and the microstructure show the regions to be fully

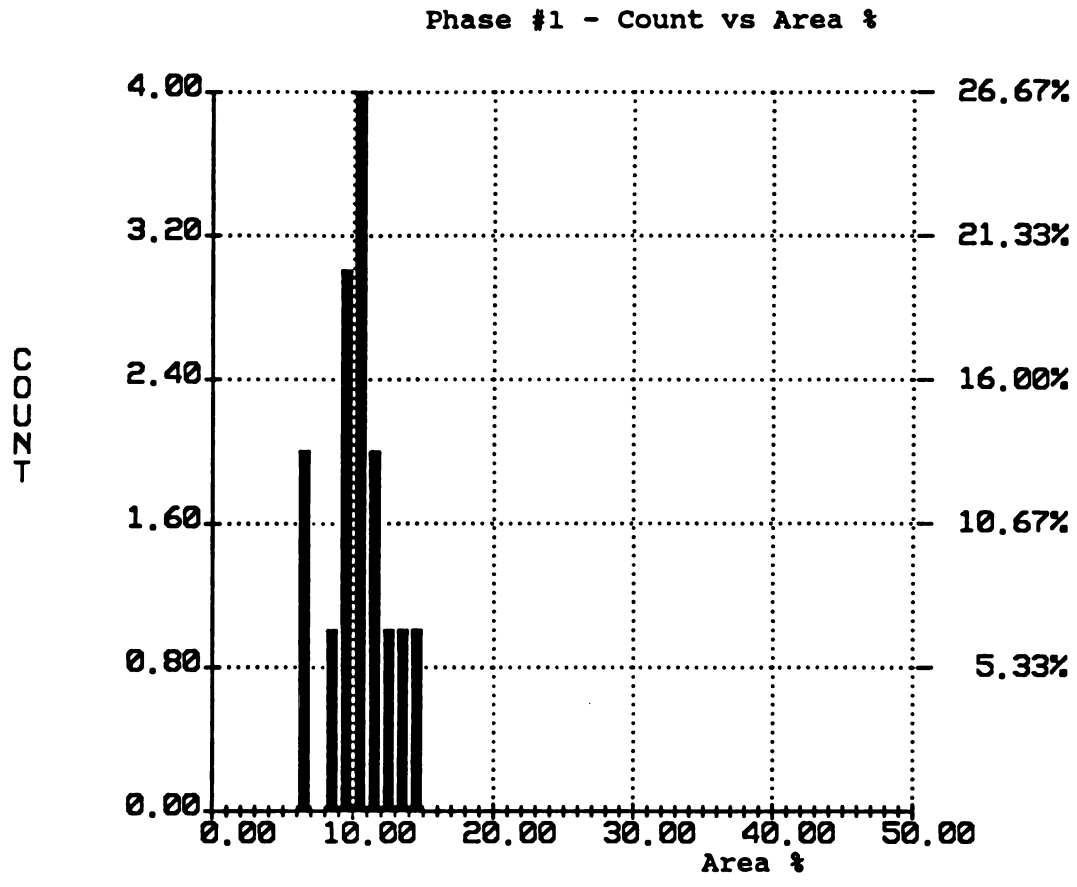

Average	:	10.408
Standard Deviation	:	2.214
Fields analyzed	:	15
Field area	:	1.639e+06 mic^2
Total area surveyed	:	2.458e+07 mic^2

Figure 41. Histogram representing the fiber volume fraction of the 2″ × 6″ (50 mm × 150 mm) plate and 2″ × 2″ (50 mm × 50 mm).

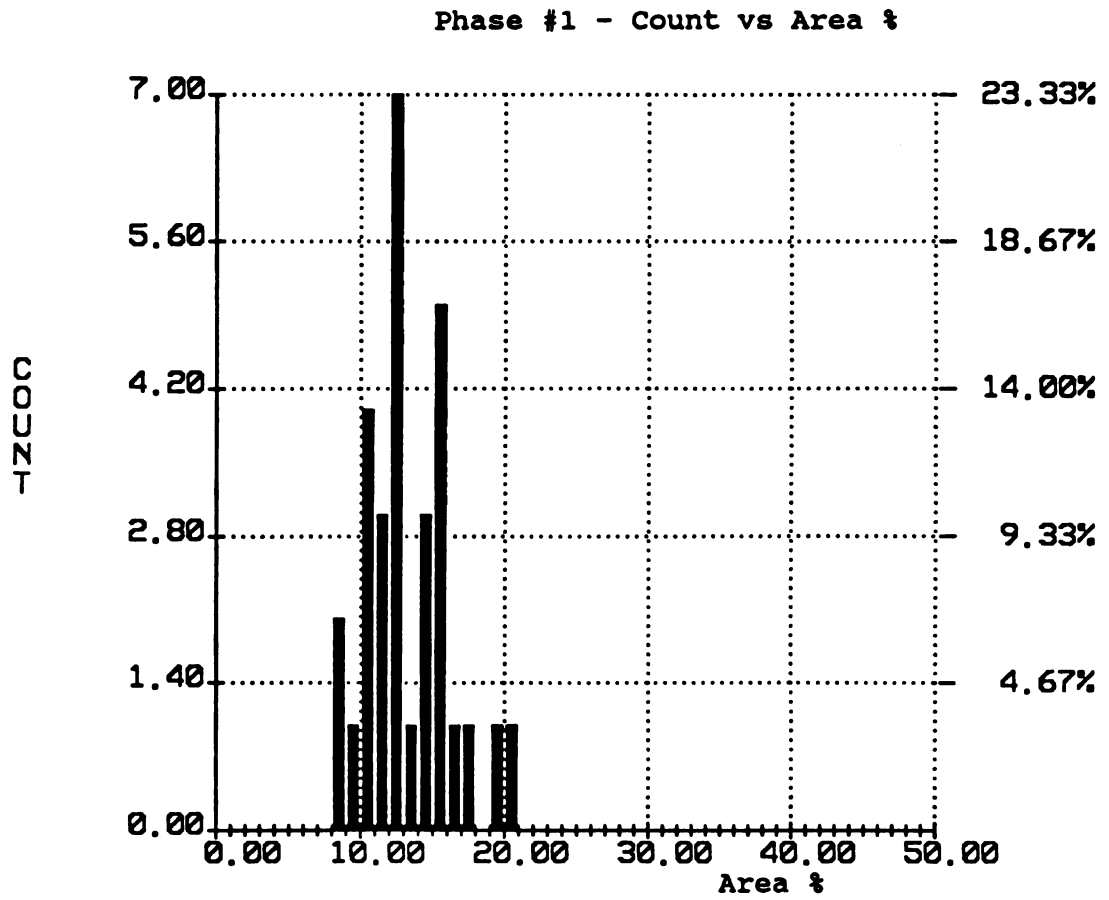

Average	:	13.323
Standard Deviation	:	2.866
Fields analyzed	:	30
Field area	:	1.639e+06 mic^2
Total area surveyed	:	4.916e+07 mic^2

Figure 42. Histogram representing the fiber volume fraction of the 2″ × 8″ (50 mm × 200 mm) plate.

consolidated. Porosity is still evident in some portions of the plate but distributed throughout the matrix away from the fiber.

Mechanical Testing

Five specimens were tensile tested at room temperature. One test from this batch was thrown out because of a computer malfunction. The reason for the limited amount of specimens was because only three plates were hot pressed that were large enough to make tensile bars. With these being the first specimens produced using this process, the focus was placed more on the microstructure evaluation to see if the process actually worked. The stress-strain curves for the four successful tests are shown in Figure 43. The curves display a variation in tensile strength from approximately 850 MPa to 250 MPa. The values are shown in Table 3.

The composite processed manually with 8% fiber reinforcement displayed a yield strength of approximately 650 MPa. The ultimate tensile strength was 766 MPa and the tensile elongation approximately 2%. The modulus value obtained from the test was 241 GPa. The values for monolithic hot pressed FeCrAlY [90] are also given in Table 3. The strength of the FeCrAlY for the samples containing 8% and 13% fiber volume fraction has been improved significantly by the reinforcements. Using a room temperature strength of 1380 MPa for FP fibers, ROM calculations (Eq. 2.11) predicted a composite strength of 596 MPa (the matrix strength at the fiber failure strain is used). For a fiber failure strain of 0.4% [80], the strength of the matrix is at approximately the yield strength, which is 528 MPa. The actual strength of the composite is much greater indicating the strain hardening of the matrix contributed to the strengthening of the composite as well. Using Equation 2.10, ROM predicted a UTS of 727 MPa. In both cases the measured

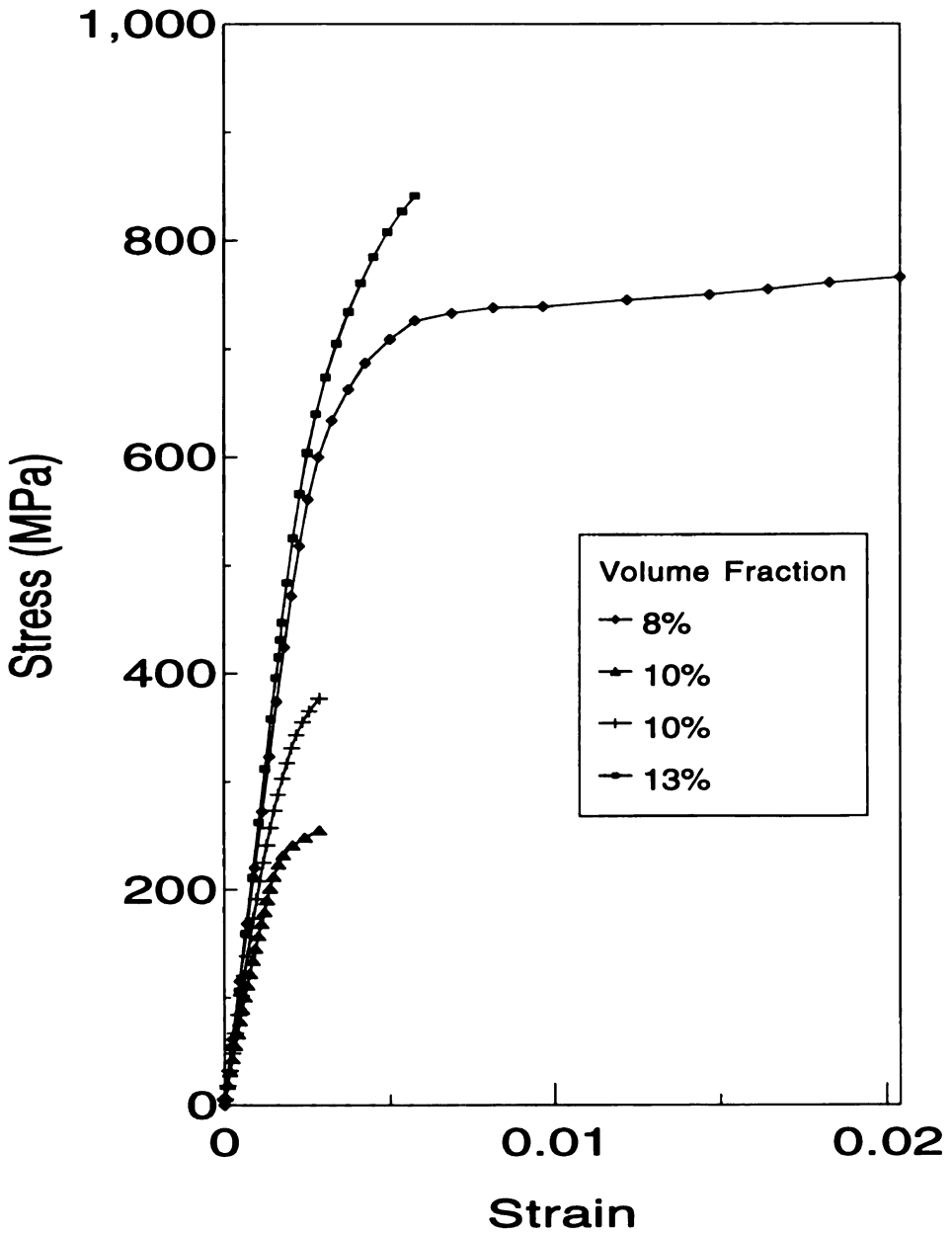

Figure 43. Plot of Stress Strain values for FeCrAlY/Al_2O_3 composites

Table 4. Tensile properties of -325 mesh FeCrAlY/Al_2O_3

Specimen Type	V_f	Porosity	YS (MPa)	UTS (MPa)	ROM (Eq. 2.11)	ROM (Eq. 2.10)	%ROM (Eq.2.11)	E (GPa)	Elong.%
Matrix	0	-------	528 ± 23	670 ± 19	-------	-------	-------	234 ± 10	6
Manually Coated	8	1.2%	650	766	596	727	129	245	2
Wound (2″ × 8″)	13	1.0%	800	841	639	762	132	252	0.5
Wound (2″ × 6″)	10	1.6%	220	255	613	741	42	249	0.3
Wound (2″ × 6″)	10	1.6%	331	377	613	741	62	249	0.3

values exceeded the predicted amount.

The composites produced by winding show significant differences. The specimen from the 2″ × 8″ (50 mm × 200 mm) plate displayed a much higher tensile strength of 841 MPa and yield strength of approximately 800 MPa. The strength increase corresponds to an increase in reinforcement. The volume fraction for this specimen was 13%. There also was a decrease in elongation to approximately 0.6%.

This difference in values between ROM and the observed could be attributed to reasons previously mentioned in the literature review such as the variability fiber strength and reactions at the fiber matrix interface. In addition, the microstructure shows an uneven distribution and it is possible that areas within the tensile gauge contain more fibers. The image analysis measurement gives a mean value so some field measurements will be higher. However, the measurements from the image analyzer provide a value representative of the entire plate which corresponds to the close agreement with the density measurements.

The specimens from the 2″ × 6″ (50 mm × 150 mm) plate which contained a fiber volume fraction of 10% failed at much lower strengths than predicted. This premature failure can traced directly to porosity as shown in Figure 46.

Figures 44-46 show the fracture surfaces from the tensile specimens. The fracture surface from the manually processed sample is shown in Figure 44. It shows some fiber pullout and plastic flow around the fibers. There is also noticeable plastic deformation in areas lacking fibers. The fracture surface from the specimen containing 13% fiber volume fraction is shown in Figure 45. There is limited fiber pullout and noticeable deformation in areas of fewer fibers as shown in Figure 44. These features are consistent with the critical

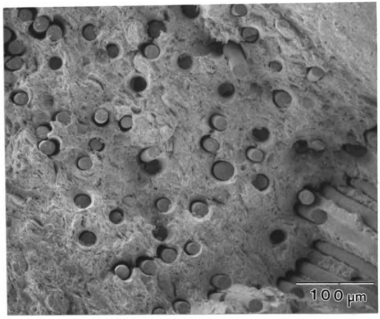

Figure 44. Fracture surface from manually processed sample. Fiber volume fraction is approximately 8%. The UTS of the specimen was 766 MPa and exceeded ROM by 29%.

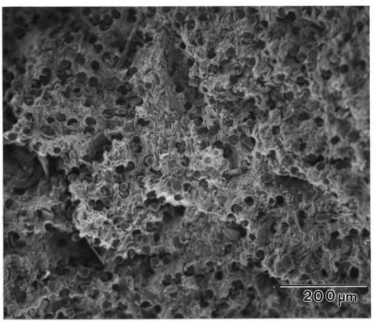

Figure 45. Fracture surface from specimen containing 13% fiber volume fraction. Specimen was fabricated using the filament winding machine. The UTS of the specimen was 841 MPa and exceeded ROM by 32%.

length calculations discussed in the previous section.The distribution of the 13% fiber volume fraction sample is much improved due to the winding process.

The fracture surface representing the wound samples which failed at low strengths is shown in Figure 46. The SEM micrograph in Figure 46 shows a porous area near fibers clumped together as indicated by the arrows. There are also areas in which the FeCrAlY does not appear to be fully consolidated.

The results of the study at this point indicate that the process needs improvement in consistency of the lay-up, the fiber volume fraction, and the consolidation parameters to minimize the fiber damage and achieve maximum density. However, the results provided several positive indications. The microstructures showed that the colloidal suspension process was successful in infiltrating the fibers without a binder. The fibers were separated and the matrix particles were indeed attracted to individual fibers. Improvements in volume fraction and fiber distribution were shown in samples produced by automatically winding the fibers through the suspension. In addition fiber alignment was improved by using the filament winding machine.

The mechanical was testing was inconclusive because of the number of specimens and the variation in microstructural features and defects. However, the results are encouraging because two of the samples showed better than ROM strength even though there was porosity and fiber damage in portions of the plate from which they were produced. With a better process control it could be anticipated that improved mechanical properties could be obtained using this process.

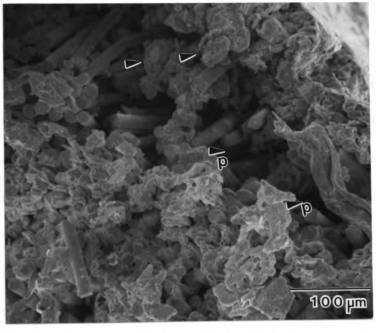

Figure 46. Fracture surface from specimen containing 10% fiber volume fraction showing porosity and areas which appear to be partially consolidated indicated by arrows. The UTS of the specimen was 255 MPa and 42% ROM.

4.3 Consolidated Specimens, -500 Mesh Matrix Powder

Steps were taken to optimize the fabrication process. First, a smaller size, -500 mesh (6.8 μm ± 4.4 μm) FeCrAlY powder was obtained to increase the fiber volume fraction. A smaller size powder would decrease the area in between fibers. In addition, the winding system's bath design was modified to improve efficiency. The pressing parameters were varied to minimize fiber damage and achieve full consolidation. This included slow ramping to the consolidation pressure and utilizing different pressures. In the earlier experiments, it was determined that the consolidation pressure was being applied over two minutes. This had not been taken into consideration when the hot press schedules were evaluated. Loads applied quickly during the early stages of consolidation are more likely to create stress concentrations when the matrix is not sufficiently deformable [42]. Smaller size specimens (2″ × 2″ (50 mm × 150 mm)) were used for this part of the study to minimize material waste and because only microstructural evaluation and density measurements were performed. Two plates of approximately equal thickness (1 mm) were hot pressed for each set of conditions to try to gain consistency in the processing technique. Once the optimum parameters were determined, then larger specimens would be made for mechanical testing.

The results for this section will be divided into subsections according to the pressing parameters used. Then, separate subsections will cover the mechanical properties, and final observations.

Consolidation Parameters: 1950° F, Ramp to 7.5 ksi over 1h, Hold for 1 hour

The microstructures representing the plates processed at these parameters are shown in Figures 47 and 48. Figure 47 shows the transverse sections from each plate to be similar in distribution and volume fraction. The volume fraction of fiber has increased as result of the finer powder size of the FeCrAlY. The distribution was relatively uniform but still showed limited regions of nonuniformity. There is significant improvement in the microstructure over the previous samples processed with the -325 mesh powder. Porosity is evident in both the matrix and around the fibers. Figure 48 shows a longitudinal section. Two micrographs were used to extend the view so that the extent of the undamaged fibers could be seen. Substantial porosity is present along the fibers.

The volume fraction was measured in regions which contained lesser amounts of porosity. This was done because if pores are connected to the fiber, the image analyzer distinguishes it as one whole shape. This results in a higher volume fraction reading. The histogram in Figure 49 represents a mean volume fraction of approximately 19% and a calculated density of 6.60g/cc. This value was significantly different from the measured density which was determined to be 6.30 g/cc. This implies that the amount of porosity present is at least 5%. The extent of porosity made it difficult to use the image analyzer so only a rough approximation for the fiber volume fraction could be obtained.

Slow ramping to the consolidation pressure over one hour reduced the fiber damage significantly. However, the pressure used was too low because of the amount of the porosity present. The results did provide a good starting point in the parameter optimization and in the following sections the improvement is significant.

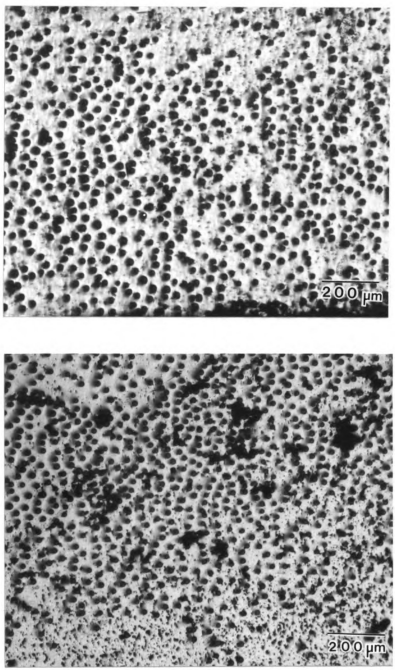

Figure 47. Transverse sections of a composite consolidated at 7.5 ksi (52MPa) using a 1h ramp to consolidation pressure. Porosity is evident in the matrix and around the fibers.

Figure 48. Extended longitudinal view of composite consolidated at 7.5 ksi (52MPa) using a 1h ramp to consolidation pressure. No fiber damage is apparent, but there is porosity along the fiber.

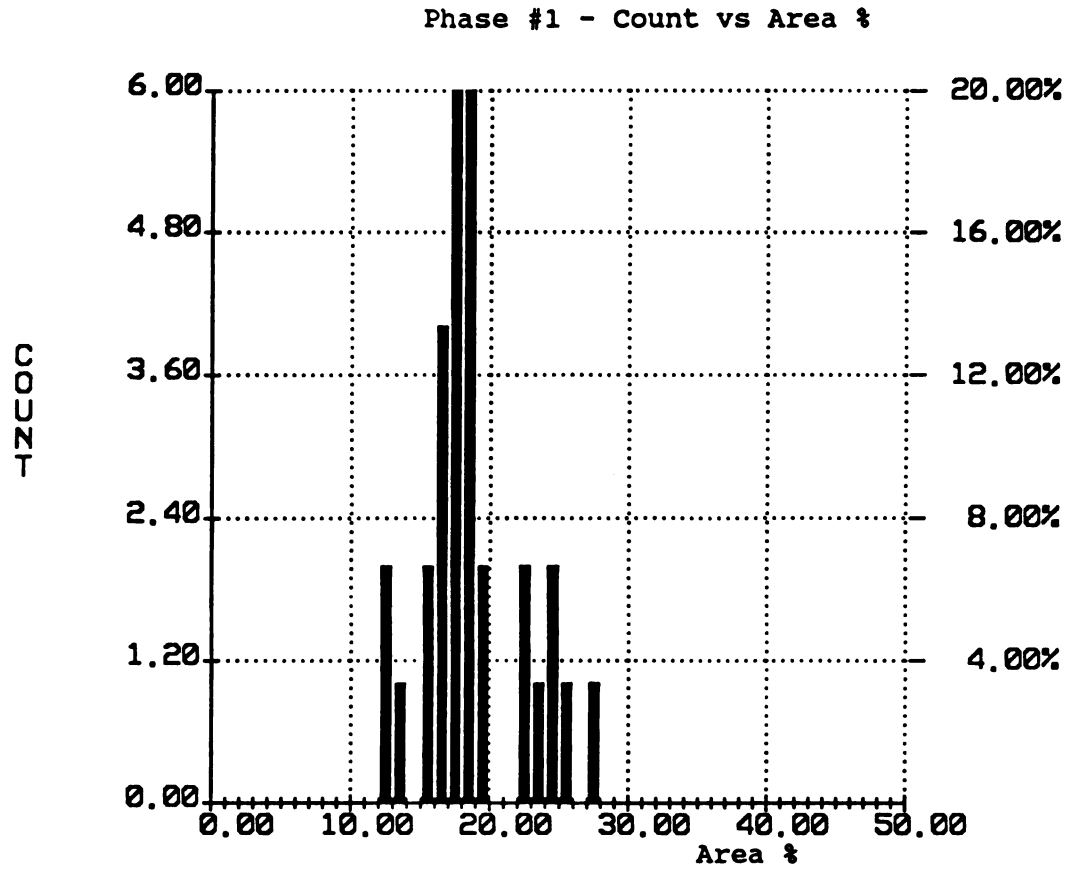

Average	:	18.608
Standard Deviation	:	3.588
Fields analyzed	:	30
Field area	:	1.639e+06 mic^2
Total area surveyed	:	4.916e+07 mic^2

Figure 49. Histogram representing fiber volume fraction of composite processed at 7.5 ksi (52 MPa) using a 1h ramp to consolidation pressure.

Consolidation Parameters: 1950° F, Ramp to 10 ksi over 1h, Hold for 1 hour

Increasing the consolidation pressure to 10 ksi (69 MPa) resulted in the microstructures shown in Figures 50 and 51. The transverse sections in Figure 50 show a more dense composite. The distribution is similar to the specimen consolidated at 7.5 ksi (52 MPa) and the volume fraction is approximately the same indicating that some consistency was maintained in the processing. Although the distribution is uneven in some areas, the fibers do not touch. The longitudinal section in Figure 51 displays no fiber damage and only slight porosity in the matrix.

The volume fraction histogram is shown in Figure 52. The mean value is approximately 17%. and the calculated density is 6.66 g/cc. Density measurements gave a value of 6.56 g/cc which corresponds to a porosity of approximately 1.5%.

The results from this section are a significant improvement over the plates processed at 7.5 ksi (52 MPa). The porosity value, although small is still a concern, especially in a central region as shown in Figures 36 (b) and 46 and the corresponding strengths.

Consolidation Parameters: 1950° F, Ramp to 15 ksi over 1h, Hold for 1 hour

The microstructures in Figures 53 and 54 show the greatest improvement. The transverse sections in Figure 53 show a higher volume fraction. The distribution remains uneven in limited areas but the fibers do not touch each other in regions containing a higher fiber volume. Most noticeably there is a matrix region near the bottom of the section. The transverse section in Figure 54 shows aligned fibers and the matrix to be fully dense. There are some fiber breaks but these breaks are not typical. The segments are much longer indicating it is suitable for maximum load transfer.

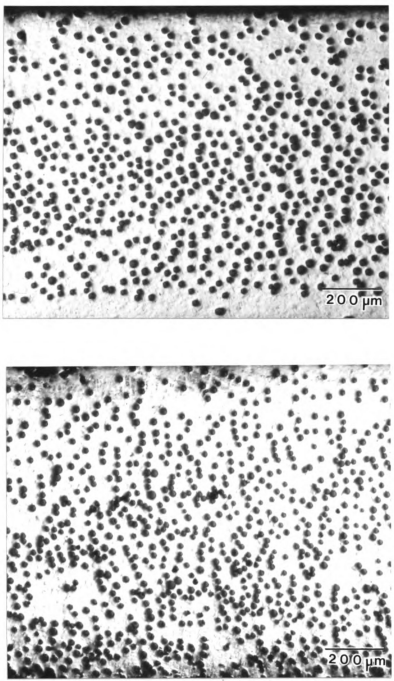

Figure 50. Transverse sections of a composite consolidated at 10 ksi (69 MPa) using a 1h ramp to consolidation pressure showing features similar to Figure 47.

Figure 51. Longitudinal sections of a composite consolidated at 10 ksi (69 MPa) using a 1h ramp to consolidation pressure. There is slight porosity in the matrix.

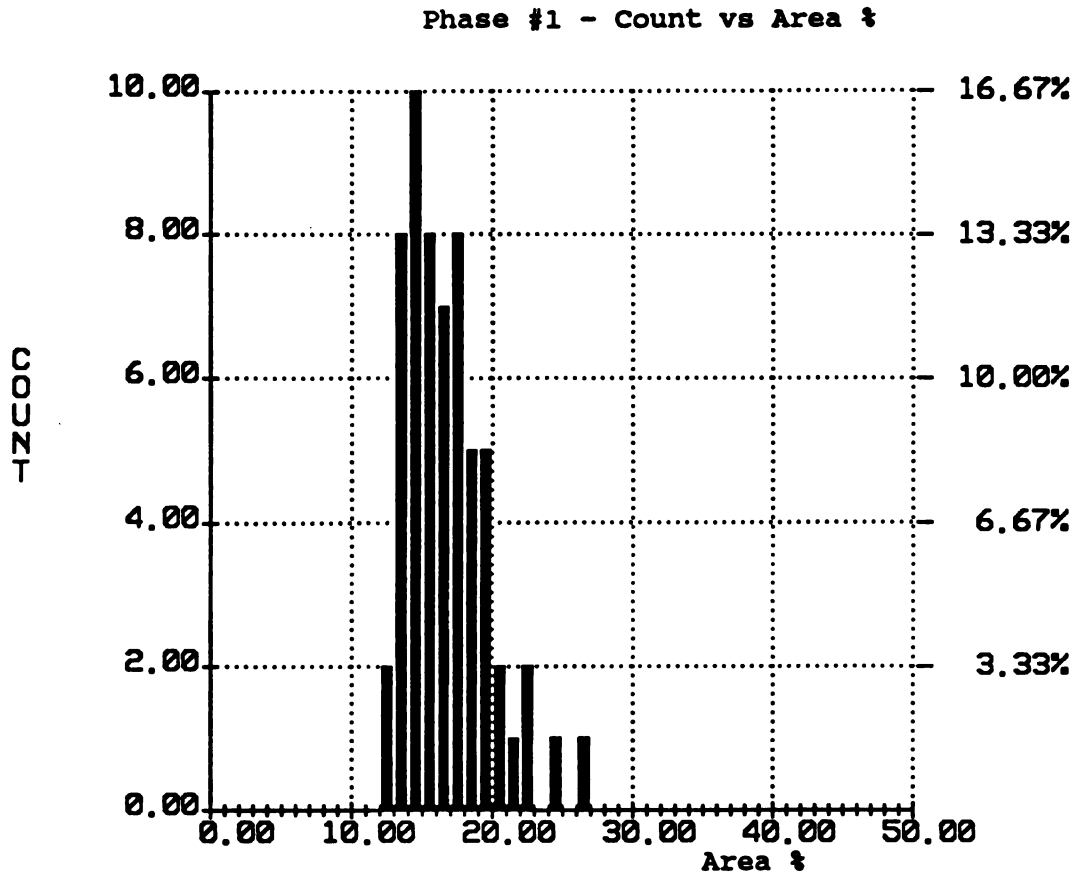

Average	:	16.787
Standard Deviation	:	2.900
Fields analyzed	:	60
Field area	:	1.639e+06 mic^2
Total area surveyed	:	9.833e+07 mic^2

Figure 52. Histogram representing fiber volume fraction of specimen consolidated at 10 ksi (69 MPa) using a 1h ramp to consolidation pressure.

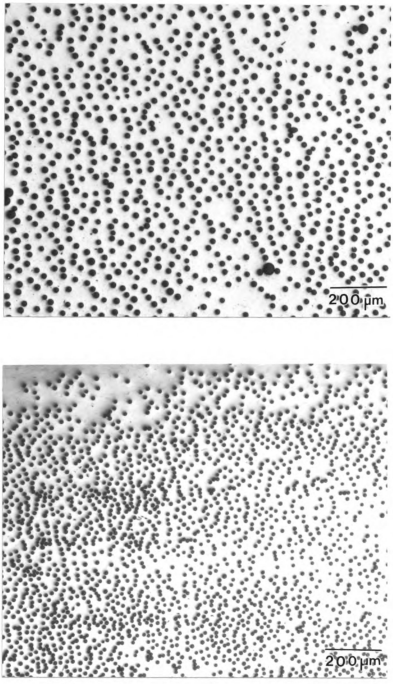

Figure 53. Transverse sections of a composite consolidated at 15 ksi (103 MPa) using a 1h ramp to consolidation pressure showing increased fiber volume fraction and improved distribution.

Figure 54. Longitudinal sections of a composite consolidated at 15ksi (103 MPa) using a 1h ramp to consolidation pressure showing minimal fiber damage and excellent consolidation.

The histogram in Figure 55 represents a fiber volume fraction of approximately 21% and the calculated density is 6.52 g/cc. The measured density was 6.5 g/cc. The density values showed excellent agreement and are almost exact. Thus, this specimen is fully consolidated. These observations indicated a suitable set of parameters for consolidating specimens for tensile testing.

The preceding results indicated that the optimum hot pressing parameters were slow ramping to 15 ksi (103 MPa) over 1 hour, and holding for one hour at 1950° F (1066° C). Also, the use of a smaller size matrix powder increased the volume fraction significantly and improved the distribution. However, there still remained limited areas of unevenness in the distribution. One common feature was matrix dominated areas near the top or bottom edge of the specimen. As previously mentioned, the uneven suspension placements above and below the ply probably account for this feature.

Another factor to consider is what happens to the specimen after it been placed in the rings. The sample at this point is wet. The ply is laid in the ring assembly over a layer of extra suspension which is evenly spread on the face sheet. Then extra suspension is placed on top of the ply. Some material is lost during handling so suspension is placed on areas lacking and then spread evenly. The interparticle forces still act as long as the sample is wet. Once the top face sheet is in place, the sample is carefully put away to transport it to NASA LeRC by automobile. By this time the green plates are dry and fragile. Coating experiments have shown the slightest touch to knock the powder off. In some cases, vibration from a carbon coater has knocked the powder off the fibers. It is possible the vibrations from the automobile during the road trip can cause some of the matrix to shift to the bottom.

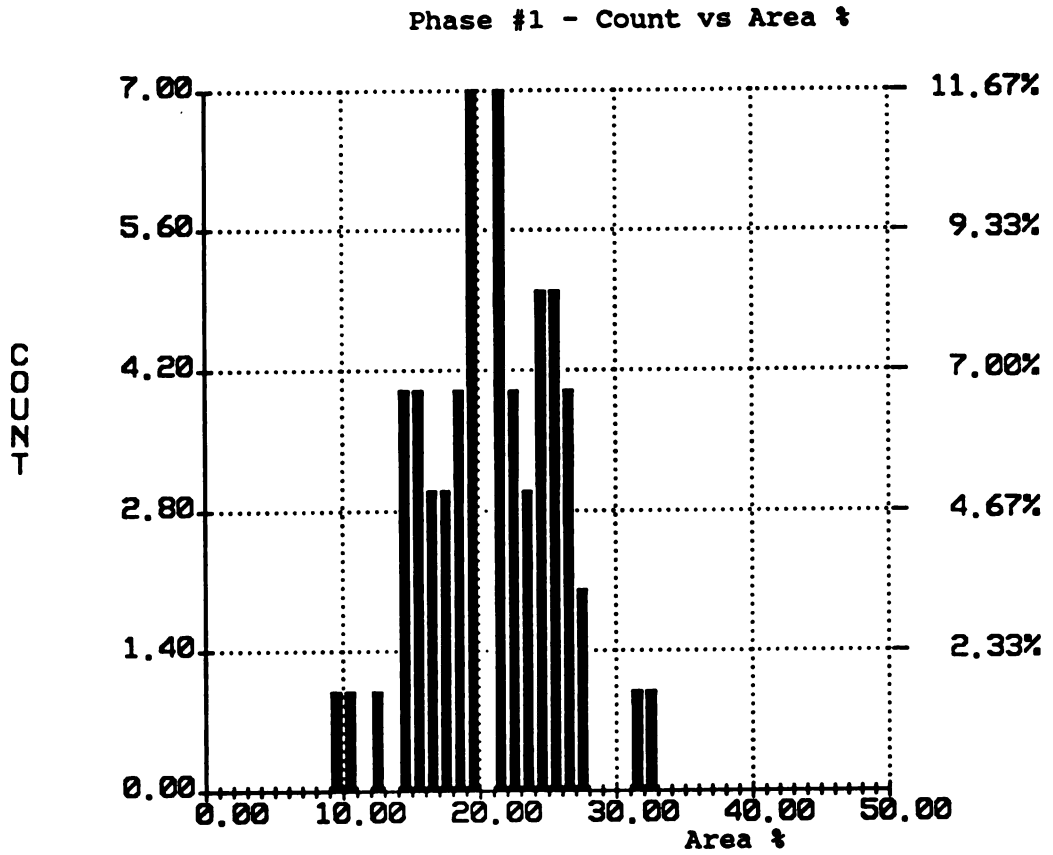

Average	:	20.898
Standard Deviation	:	4.894
Fields analyzed	:	60
Field area	:	1.639e+06 mic^2
Total area surveyed	:	9.833e+07 mic^2

Figure 55. Histogram representing fiber volume fraction of specimen consolidated at 15 ksi (103 MPa) using a 1h ramp to consolidation pressure.

Mechanical Testing

Five 2″ × 6″ (50 mm × 150 mm) plates were hot pressed using the optimum parameters and three tensile bars were machined from each plate. Only eleven tests were run because the other samples broke during machining which indicated something was wrong with some of the plates. Table 5 shows the strength values obtained from the tests. All the specimens failed at low strengths and very low strains, less than that of the fiber failure strain. The data also shows a substantial deviation in strength. There was a strength increase at 1100 K compared to the unreinforced FeCrAlY value of 51 MPa [90]. However, at this temperature, the fiber is the main source of strength. Though the composite strength was higher, the fibers failed at a low load and strain. This type of behavior was also exhibited in a Saphikon fiber reinforced FeCrAlY composite investigated by Draper et. al [90].

The reason for these low strength values can be seen in the fracture surfaces in Figure 56 (a) and 56 (b). Figure 56 (a) displays limited fiber pullout and ductility similar to the fracture surfaces in Section 4.2. The fibers are also well distributed. Figure 56 (b) shows a region of unconsolidated FeCrAlY particles indicating that the specimens were not fully consolidated. Every specimen contained areas similar to these. This also explained why some specimens broke during machining.

The results clearly were not reflective of the processing parameters and the lay up process had been identical to the previous ones. The plates were hot pressed using a different press. However, the parameters used were the same and should not have had any bearing on the results.

A decision was made to hot press 3 more plates under the same conditions and then

Table 5. Tensile Properties of -500 mesh FeCrAlY/Al_2O_3.
Fiber volume fraction is approximately 18%.

Temperature Tested	Matrix UTS (MPa)	UTS (MPa)	ROM (MPa) Eq. 2.11	%ROM	% Elong
Room	670	296 ± 136	681	41	0.15 ± 0.07
700 K	520	209 ± 127	576	36	0.3 ± 0.2
1100K	50	99 ± 28	281	35	0.2 ± 0.2

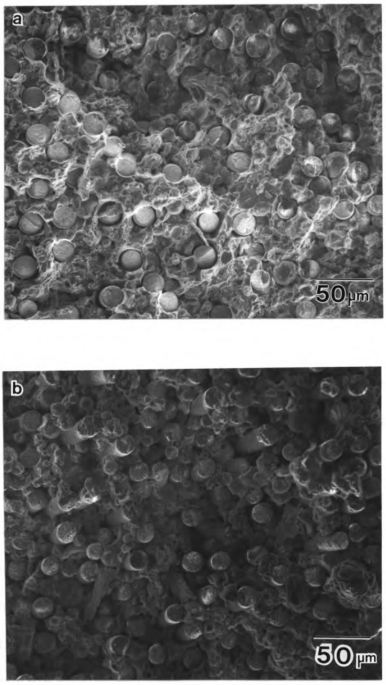

Figure 56. Fracture surfaces representing the tensile specimens processed under optimum conditions showing consolidated (a) and unconsolidated regions (b).

HIP them using the same parameters to see if that would remedy the problem. After the samples were consolidated, it was discovered that the vacuum hot press used to consolidate the specimens was calibrated incorrectly. The hydraulic line which supplies the pressure was not connected properly. This resulted in a false pressure reading. Instead of 15 ksi (103 MPa), the actual pressure applied was approximately 5 ksi (34 MPa) [91].

Of the 3 plates, only one was used for tensile testing. One plate was severely bowed and could not be machined and other plate produced bowed tensile bars which were not tested because they were deformed slightly. The bowing out occurred during the HIP cycle and is attributed to nonuniformities or irregularities in the material [91]. NDE was performed on the specimens and the results verified the nonuniformities. If the plate underwent an initially bad hot press run, it is probable these nonuniformities were created during the hot pressing sequence and then magnified with the HIP. However, the fracture surface from a tensile specimen in Figure 57 displays a similar distribution to the one in Figure 52, uneven area near the edge of the specimen with regions of excellent distribution as shown in Figure 58. The fracture surface is planar with areas of limited fiber pullout and appears consistent with the critical length calculations. The composite also appears to be fully dense. The measured density was 6.61 g/cc indicating a fiber volume fraction of approximately 18%. These fiber volume fractions are consistent with the previous samples. The UTS values from the specimens were similar and the strength was reported at approximately 614 MPa and an elongation of approximately 0.6% at room temperature. This compares to a ROM UTS (Eq. 2.11) value of 681 MPa. This measured value is within 10% of the predicted value. Despite the inconsistencies in the consolidation the microstructures, the fiber volume fraction and minimal fiber damage remained consistent.

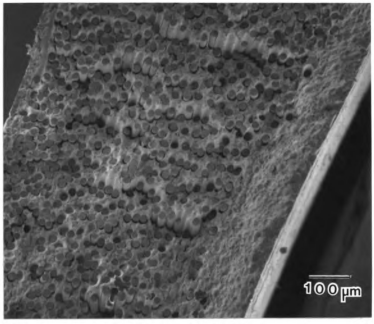

Figure 57. Fracture surface of a composite hot pressed and HIPed at optimum parameters. Fiber volume fraction is approximately 18%. The UTS is 614 MPa and 90% ROM.

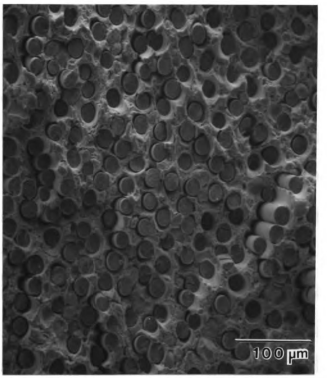

Figure 58. Fracture surface of composite hot pressed then HIPed at optimum parameters. showing a region containing an excellent fiber distribution with limited fiber pullout.

5. CONCLUSIONS

FeCrAlY matrix composites reinforced with continuous fine diameter Al_2O_3 fibers have been successfully produced and consolidated using a colloidal suspension process without an organic binder. This was accomplished by adjusting the pH of the suspension in accordance with predictions of a suspension stability program which utilized zeta potential data to predict suspension stability for the fibers with respect to themselves and instability or heterocoagulation for the composite system. Fiber coating experiments showed the fiber tow to be thoroughly infiltrated with the matrix at a pH of 6. Two types of matrix powders with different morphologies were used, an irregular shaped -325 mesh (32 $\mu m \pm 13.15$ μm) powder and a finer, spherical -500 mesh (6.8 $\mu m \pm 4.4$ μm) powder.

Initial specimens were consolidated using the -325 mesh (32 $\mu m \pm 13.15$ μm) powder. The composites were characterized by a low fiber volume fraction, a non-uniform distribution and some regions containing porosity. Porosity was identified by X-Ray radiography and determined to be approximately 1-2%. Longitudinally, the specimens contained regions of wavy fibers, aligned fibers and damaged fibers. A comparison was drawn between a manually processed sample and several processed by winding the tows through the suspension automatically. The fiber volume fraction was increased and the fiber distribution was improved using the winding system. Preliminary tensile test results showed a variation in data. Two specimens contained porosity and failed at low strengths and the UTS of two specimens exceeded ROM predictions.

A smaller size powder was used to increase the fiber volume fraction and the hot pressing schedule was varied to determine optimum parameters that would produce a fully dense composite with minimal fiber damage.

The difference in morphology and size of the matrix powders had a significant effect on the composites. Changing to a smaller, spherical powder improved the fiber coating which led to increases in volume fraction from 13% to 21%. The fiber distribution was significantly improved yet there still remained some uneven areas. However, the microstructural features were common in all specimens indicating some consistency was maintained in the lay up process.

The optimum hot pressing parameters were determined to be 1950° F (1063° C), 15 ksi (103 MPa) with a 1 hour ramp to consolidation pressure, and hold at temperature and pressure for one hour. The microstructures exhibited minimal fiber damage as a result of ramping to the consolidation pressure. Density measurements and volume fraction measurements showed the composite to be fully consolidated.

Plates were hot pressed at the optimum parameters and tensile bars were machined and tested. The specimens failed at low strengths for all conditions. Fracture surfaces revealed regions of well consolidate areas and regions of unconsolidated or partially consolidated matrix particles which contributed to the failure of the composites.

An additional set of plates were hot pressed and then HIPed so complete consolidation could be achieved. The HIP parameters used were the same as those used for the hot pressing stage. Two of the three plates were deformed during the HIP cycle due to non-uniformities in the composite. It was later found out that the hot pressing was not carried out at the proper pressure due to an equipment error. The actual pressure used was approximately one third of that required. This would account for the unconsolidated regions in the previous plates which exhibited the poor mechanical properties.

The main goal of this project was to produce a fine diameter fiber reinforced metal

matrix composite using the colloidal suspension process. However, mechanical testing results showed a large variation as a result of poor consolidation control. Although the microstructures were consistent, some more improvements need to be made in the lay up and handling of the green composite. Modifications were made to the filament winding system throughout the course of the project and these improvements made the lay-up process less time consuming. However, problems still existed in keeping the particles suspended. Lastly, the consolidation process must be kept consistent. Optimum parameters were chosen, but the parameters' effect on the mechanical properties could not be evaluated due to inconsistent consolidation.

6. RECOMMENDATIONS FOR FUTURE WORK

The winding process can be improved by making sure the delivery spool and take up mandrel operate in sync. The current modification does work, but the delivery spool rotates slightly faster than mandrel and the rotational speed of the ball mill. This causes too much slack in the tow occasionally and the rotational ball mill it is attached to has to be turned off and on periodically. Installing a motor on the delivery spool similar to the one on the mandrel and connecting it to a power supply would allow them to rotate in sync. However, this would necessitate another power supply. Another option would be to connect the spool to the mandrel by means of a belt similar to the current design. This way would be cheaper but would require more tinkering. With even tension between the delivery spool and take up mandrel, the suspension can be monitored more effectively.

The particles must be kept in suspension to so that the fibers may be continuously coated. This is difficult because the particles settle out rapidly due to their high density. Stirring the suspension periodically helps but it also interferes with the process. Implementing some mechanical device that could run across the bottom of the suspension back and forth evenly would keep the suspension from settling down and becoming thick. With these minor adjustments, the winding process should be able to operate smoothly with no interruptions.

An improvement must be made in the removal of the ply from the mandrel, its placement into the ring assembly, and handling of the green specimen until it is in the hot press. This part of the process is the most difficult because of the fragile nature of the specimen. Problems occur when the extra suspension is placed above and below the plys. This is difficult to quantify because of slight differences in the specimens. Some required more

material than others as a result of inconsistent winding (the interruptions). It is anticipated that a quantification of some sort can be accomplished if the adjustments to the winding system are made. A better approach would be to use foils instead, but the material is not available in foil form. The samples can be kept wet until they are transported. However, it is not known how long it takes before the sample dries to a point where it becomes extremely fragile.

The consolidation has been carried out at NASA Lewis Research Center as part of the research grant and because the facilities required to consolidate specimens of the dimensions used for this study are not available at the university. The samples had to be transported there by automobile and then there was a wait for them to be consolidated because of priority considerations. This created a long turnaround time. Difficulties were experienced due to the long turnaround time because it prohibited testing a wider range of processing parameters. In addition, there was equipment downtime and then miscalibration of the equipment which damaged two batches of samples. This precluded our ability to obtain adequate results. If a smaller sample size can be used for mechanical testing, it may be possible to consolidate the specimens here in a more timely manner and have more control over the consolidation process.

7. REFERENCES

1. K.K. Chawla, Composite Materials, Springer Velag, New York, 1987.

2. W.H. Dresher, " The Age of Fibers", *JOM*, (4), p.17, 1969.

3. F.K. Ko, "Preform Fiber Architecture for Ceramic Matrix Composites", *Ceramic Bulletin*, **68** (2), 1989.

4. H. D. Stephens, H. Kern, J. Jonczak, " Bteween Dreams and Reality of MMCs - A Big Gap?", Advanced Composites 93: Proceedings of the International Conference on Advanced Composite Materials, T. Chadra, A.K. Dhingra, eds. p.951, TMS 1993.

5. H. Lilholt, " Strengthening Mechanisms", Mechanical Properties of Metalllic Composites, S. Ohchiai, ed. Marcell Decker Inc., New York, 1994.

6. H.L.Cox, "The Elasiticity and Strength of Paper and Other Fibrous Materials", *Br. J. Appl. Phys,*. **3**, p. 72, 1952.

7. A. Kelly, Strong Solids 2nd ed. , Claredon Press, Oxford University Press, 1973.

8. M.R. Piggot, Load Bearing Fiber Composites, Pergamon Press, Oxford, 1980.

9. H. W. Rauch Sr., W. H. Sutton, L. R. McCreight, Ceramic Fibers and Fibrous Composite Materials, Acadamic Press, New York, 1968.

10. A. Kelly, G. Davies, " The Principles of the Fiber Reinforcement of Metals", *Metals Rev.*, **10**, (37), p.1, 1965.

11. G. E. Deiter, Mechanical Metallurgy, 3rd ed. McGraw Hill, Inc., New York, 1986.

12. G. H. Holister, C. Thomas, Fibre Reinforced Materials, Elsevier Publishing Co LTD., Amsterdam, 1966.

13. M. Taya, R.J. Arsenault, Metal Matrix Composites: Thermomechanical Behavior, Pergamon Press, New York, 1990.

14. A. Kelly, W.R. Tyson, "Tensile Properties of Fiber Reinforced Metals: Copper/Tungsten and Copper/Molybdenum", *J. Mech. Phys. Solids*, **13**, p.320, 1965.

15. D. L. McDaniels, R. W. Jech, J. W. Weeton, " Analysis of Stress Strain Behavior of Tungsten- Fiber- Reinforced Copper Composites", Transactions of AIME, **233**, (4), p.636, 1965.

16. R. K. Everett, R. J. Arsenault, Metal Matrix Composites: Mechanisms and Properties, Academic Press, Boston, 1990.

17. W.A. Curtin, "Ultimate Strengths of Fibre-Reinforced Ceramics and Metals", *Composites*, **24**, (2), 1993.

18. R. W. Rice, " Mechanisms of Toughening in CMCs", Proceedings of the 5th Annual Conference on Composites and Advanced Ceramic Materials, American Ceramic Society Inc., 1981.

19. A.G. Evans, " The Mechanical Properties of Reinforced Ceramic, Metal, and Intermetallic Matrix Composites", *Mat. Sci. Eng.* **A143**, p.63, 1991.

20. A.G. Evans, D. B. Marshall, " The Mechanical Behavior of Ceramic Matrix Composites", *Acta Metall.*, **37**, (10), p. 2567, 1989.

21. M. D. Thouless, A.G. Evans, "Effects of Pull-Out On The Mehcanical Properties Of Ceramic Matrix Composites", *Acta Metall.*, **36**, (3), p.517, 1988.

22. J. A. DiCarlo, "Fibers For Structurally Reliable Metal and Ceramic Composites", *JOM*, (6), p.44., 1985.

23. C. M. Friend, "Toughness in Metall Matrix Composites", *Mat. Sci. Tech.* **5**, (1), p.1, 1989.

24. M. D. Thouless, O. Sbaizero, L. S. Sigl, A.G. Evans, "Effect of Interface Mechanical Properties on Pullout in a SiC-Fiber-Reinforced Lithium Aluminun Silicate Glass Ceramic", *J. Am. Cer. Soc.*, **72**, (4), p. 525, 1989.

25. A.G. Evans, R. M. McMeeking, "On The Toughening of Ceramics By Strong Reinforcements", *Acta Metall.*, **34**, (12), p.2435, 1986.

26. D. B. Marshall, B. N. Cox, A.G. Evans, "The Mechanics of Matrix Cracking In Brittle-Matrix Fiber Composites", *Acta Metall.*, **33**, (11), p.2013, 1985.

27. D. B. Marshall, B. N. Cox, "Tensile Fracture Of Brittle Matrix Composites: Influence of Fiber Strength", *Acta Metall.*, **35**, (11), p.2607, 1987.

28. N. Eustathopoulos, A. Mortenson, " Capillary Phenomena, Interfacial Bonding, and Reactivity", Fundamentals of Metal Matrix Composites, S. Suresh, A. Mortenson, A. Needleman, eds., Butterworth-Heinemann, Boston, 1993.

29. R. A. Signorelli, D. L. McDaniels, NASA TN D8204 (1976).

30. M. A. Crimp, M. J. Crimp, R.E.F.Technical Proposal, 1991.

31. S. Ochiai, "Present Status and Future of Fiber-Reinforced Metal Matrix Composites", Proceedings of The Thirty-Sixth Japan Congress on Materials Research, Japan Society of Materials Science, Kyoto Japan, 1993.

32. S. Ochiai, K. Osamura, "Influences of Matrix Ductility, Interfacial Bonding Strength, and Fiber Volume Fraction on Tensile Strength of Unidirectional Metal Matrix Composite", *Met. Trans. A.*, **21A**, (4), p. 971, 1990.

33. S. Ochiai, K. Osamura,"Influences of Interfacial Bonding Strength and Scatter of, Fiber Strength on Tensile behavior of Unidirectional Metal Matrix Composites", *J. Mat. Sci.*, **23**, p. 886, 1988

34. S. Ochiai, K. Osamura, "Tensile Strength of Fibre-Reinforced Metal Matrix Composites With Non-Uniform Fibre Spacing", *J. Mat. Sci.*, **23**, p. 886, 1988.

35. S. Ochiai, K. Osamura, "Stress Disturbance Due To Broken Fibres in Metal Matrix Composites With Non-Uniform Fibre Spacing", *J. Mat. Sci.*, **24**, p. 3865, 1989.

36. S. Ochiai, K. Osamura, "Static Stress Concentrations Due to Broken Fibres in Strain Hardenable Metal Matrix Composites Containing Elastic Fibres With Different Diameters", *Z. Metallkde.*, **79**, p.610, 1989.

37. S. Ochiai, K. Osamura, "A Monte Carlo Simulation of The Tensile Behavior of Metal Matrix Composites Containing Fibres With Different Diameters", *Z. Metallkde*, **79**, p.605, 1988.

38. S. Towata, S. Yamada, Comp 86: Recent Advances in Japan and the United States, K. Kawata, S. Umekawa, A. Koboyashi, eds. Japan Soc. Comp. Mater., Tokyo, 1986.

39. R. A. MacKay, "Effect Of Fiber Spacing On Interfacial Damage In A Metal Matrix Composite", *Scripta Met.*, **24**, p.167, 1990.

40. M. A. Wright, B. D. Intwala, "The Effect Of Elevated Temperatures on The Mechanical Properties of B-Al Composites", *J. Mat. Sci.*, **8**, p. 957, 1973.

41. T. Kyono, I. W. Hall, M. Taya, "The Effect of Isothermal Exposure On The Transverse Properties of A Continuous Fibre Metal Matrix Composite", *J. Mat. Sci.*, **21**, p.4269 1986.

42. R. K. Everett, R. J. Arsenault, Metal Matrix Composites: Processing and Interfaces, Academic Press, Boston, 1990.

43. D.W. Petrasek, D. L. McDaniels, L. J. Wesfall, J. R.Stephens, "Fiber-Reinforced Superalloy Composites Provide an Added Performance Edge", *Metal Progress*, (8), p. 27, 1986.

44. T. W. Chou, A. Kelly, A. Okura, "Fibre-reinforced Metal Matrix Composites", *Composites*, **16**, (3), p. 187, 1985.

45. R. A. MacKay, P. K. Brindley, F. H. Froes, "Continuous Fiber-Reinforced Titanium Aluminide Composites", JOM, (5), p. 23, 1991.

46. H. Kern, R.Kczmerek, J. Janczak, "Thermally Sprayed Fiber-Reinforced Metal Matrix Composites", *J. Thermal Spray Tech.*, **1**, (2), p. 137, 1992

47. P. G. Partridge, C. M. Ward-Close, "Processing os Advanced Continuous Fibre Composites: Current Practice and Potential Developments", *Int. Met. Rev.*, **38**, (1), p.1, 1993.

48. S. Nourbakhsh, O. Sahin, W.H. Rhee, H. Margolin, "Pressure Casting Of A Zirconia Alumina Fiber-Reinforced NiAl Composite", *Met. Trans. A*, **22A**, (12) p. 3059, 1991.

49. T. M. Liu, C. G. Chao, "Effect of Magnesium on Mechanical Properties of Alumina Fiber-reinforced Aluminum Composites Formed By Pressure Infiltration Casting", *Mat. Sci. Eng.*, **A169**, p.79, 1993.

50. D. M. Shah, D. L. Anton, "Alumina Fiber Reinforced Intermetallic Matrix Composites", Structural Intermetallics, R. Darolia, J. J. Lewandowski, C. T. Liu, P. L. Martin, D. B. Miracle, M. V. Nathal, p. 751, TMS, 1993.

51. S. Kohara, N. Muto, "Fabrication of SiC Fiber-Aluminum Composite Materials", Progress In Science And Engineering Of Composites Volume 2, T Hayashi, K.Kuwata, S. Umekawa, eds., p. 1451, Japan Society For Composite Materials, 1983.

52. B. A. Wilson, C. J.Suydam, M. J. Crimp, M. A. Crimp, "Processing of FeAl/Al_2O_3 IMCs Using Advanced Electrodeposition Methods", *Mat Res Soc. Symp. Proc*, **288**, p.891, 1992.

53. C. J. Suydam, "Fiber Electrophoretic Deposition Processing of Continuously Reinforced Fe-40Al/Al_2O_3 Intermetallic Matrix Composites", M. S. Thesis, Michigan State University, 1993.

54. M. J. Crimp, "Surface Characterization of Silicon Nitride and Silicon Carbide", PhD. Dissertation, Casewestern Reserve University, 1988.

55. M. J. Crimp, R. E. Johnson, J. W. Halloran, D. L. Feke, "Colloidal Behavior of Silicon Carbide and Silicon Nitride", Science of Ceramic Chemical Processing, Wiley, New York , p. 539 1986.

56. B. A. Wilson, M. S. Thesis, Michigan State University, 1992.

57. B. A. Wilson, M. J. Crimp, "Prediction of Composite Colloidal Suspension Stability Based Upon The Hogg, Healy, and Furstenau Interpretation", *Langmuir*, **9**,p.2836, 1993.

58. R. B. Bhagat, "The Effects of Hot Pressing Parameters on the Strength of Aluminum/Stainless Stell Composites", *Met. Trans. A*, **16A**, (4) p. 623, 1985.

59. P. D. Nicalou, H. R. Piehler, S. L. Semiatin, "Fiber Fracture During Processing of Continuous Fiber, Metal Matrix Composites Using the Foil-Fiber-Foil Technique", *Met. Trans. A*, **26A**, (15) p. 1129, 1995.

60. D. M. Elzey, J. F. Groves, H. N. G. Wadley, "Fiber Fracture During Consolidation of Continuously Reinforced Metal Matrix Composites", Model Based Design of Materials and Processes, E. S. Russel, D. M. Elzey, D. G. Backman, eds. TMS, p. 33, 1992.

61. J. F. Groves, D. M. Elzey, H. N. G. Wadley, "Fiber Fracture During Consolidation of Metal Matrix Composites", *Acta Metall.*, **42**, (6) P.2089, 1994.

62. D. A. Koss, J. R. Hellmann, D. F. Heaney, "Fiber Fragmentation During Processing of Metallic Matrix Composites", Submitted for Publication.

63. J. Warren, D. M. Elzey, H. N. G. Wadley, "Fiber Damage During the Consolidation of PVD Coated Ti-6Al-4V Coated Nextel 610™ Alumina Fibers", *Acta Metall.*, **43**, (10), p.3605, 1995.

64. P. C. Heimenz, Principles of Colloid and Surface Chemistry 2nd ed., Marcell Dekker Inc., New York, 1986.

65. R. J. Hunter, Foundations of Colloid Science Vol 1, Oxford University Press, New York, 1986.

66. D. J. Shaw, Introduction to Colloid and Surface Chemistry, 1980.

67. M. J. Crimp, Personal Communications

68. S. N. Heavens, "Electrophoretic Deposition as a Processing Route for Ceramics", Advanced Ceramic Processing And Technology Volume 1, J. G. P. Binner ed., Noyes Publications, New Jersey, 1990.

69. B. V. Deryguin, L. Landau, *Acta Physicochim.. URSS*, **14**, p.633, 1941.

70. E. J. W. Verwey, J. G. Overbeek, Theory Of Stability of Lyophobic Colloids, Elsevier, New York 1948.

71. R. Hogg, T. W. Healy, D. W. Furstenau, "Mutual Coagulation of Colloidal Dispersions", *Trans. Faraday Soc.*, **62**, p.1638, 1966.

72. J. M. Yang, S. M. Jeng, C. J. Yang, D. L. Anton, "Chemical Compatibility Of High Temperature Intermetallic Compounds With Various Potential Reinforcements", Mat. Res. Soc. Symp. Proc., **194**, p.365, MRS, 1990.

73. D. M. Shah, D. L. Anton, C. W. Musson, "Feasability Study Of Intermetallic Composites", Mat. Res. Soc. Symp. Proc., **194**, p.333, MRS, 1990.

74. S. L. Draper, D. J. Gaydosh, M. V. Nathal, A. K. Misra, "Compatability of Fe-40Al With Various Fibers", *J. Mat. Res.*, **5**, (9), p.1976, 1990.

75. S. L. Draper, D. J. Gaydosh, J. I. Eldridge, P. Tsui, "Development of Alumina Reinforced FeAl and FeCrAlY", HITEMP Review 1990, NASA Conf. Pub 10051.

76. C. S. Wukusick, J. F. Collins, "An Iron-Chromium-Aluminum Alloy Containing Yttrium", *Mat. Res. Stand.*, **4**, p.637, 1964.

77. C. S. Wukusick, "The Physical Metallurgy and Oxidation Behavior of FeCrAlY Alloys", GEMP-414, General Electric, 1966.

78. F. A. Golightly, F. H. Stott, G. C. Wood, "The Influence of Yttrium Additions on the Oxide Scale Adhesion to Iron Chromium Aluminum Alloy", *Oxidation of Metals*, **10**, (3) p.163, 1976.

79. F. G. Wilson, B. R. Knott, C. D. Desforges, "Preparation and Properties of Some ODS Fe-Cr-Al Alloys", *Met. Trans. A.*, **9A**, (2), p.275, 1978.

80. V. Lavaste, M. H. Berger, A. R. Bunsell, J. Besson, "Microstructure and Mechanical Properties of Alpha Alumina Based Fibers", *J. Mat. Sci.*, **30**, p.4215, 1995.

81. H. M. Yun, J. C. Goldsby, J. A. DiCarlo, "Stress-Rupture Behavior of Small Diameter Polycrystalline Alumnia Fibers", NASA Tech. Mem. 106256.

82. R. M. German, Powder Metallurgy Science, Metal Powders Industries Federation, 1984.

83. D. G. Maglaya, "Design of the Experimental Apparatus For the Fiber Electrophoretic Depositon Processing of FeAl/Al2O3 Intermetallic Matrix Composites", B.S. Thesis, Michigan State University, 1991.

84. R. Warren, Ceramic Matrix Composites, Chapman and Hall, New York, 1992.

85. W. Armstrong, M. Ramulu, M. Taya, "Fabrication of W-1% ThO2 Reinforced Fe-25Cr-8Al-0.5Y Superallot Matrix Composite", *Processing and Manufacturing of Composite Materials*, PED-Vol 49/MD-Vol. 27, p. 291, ASME, 1991,

86. D. E. Bray, R. K. Stanley, Nondestructive Evaluation: A Tool For Design, Manufacturing, and Service, McGraw-Hill, New York, 1989.

87. A. F. Bloom, P. A. Gradin, "Radiography", Nondestructive Testing of Fibre Reinforced Plastics Composites, J. Summerscales ed., Elsevier, Ney York, 1987.

88. T. W. Clyne, P. J. Withers, Introduction To Metal Matrix Composites, Cambridge University Press, London, 1993.

89. M. J. Crimp, J. Ambriz, B. A. Wilson, "Processing of FeCrAlY IMCs Using Stability Predictions", Proceedings of TMS Conference, 1994.

90. S. L. Draper, B. J. M. Aikin, J. I. Eldridge, "Tensile Behavior of Al_2O_3/FeAl+B and Al_2O_3/FeCrAlY Composites," *Met. Trans.*, **26A**, (10), 2719, 1995.

91. B. J. M. Aikin, NASA Lewis Research Center, Personal communications.